Spectral diffuse optical tomography

Suvi Källman
Master's Thesis
University of Eastern Finland
Department of Applied Physics
May 13, 2022

UNIVERSITY OF EASTERN FINLAND, Faculty of Science and Forestry, Department of Applied Physics, Computational Physics
Suvi Källman: Spectral diffuse optical tomography
Master's Thesis, 52 pages
Supervisors: professor Tanja Tarvainen, Ph.D., Meghdoot Mozumder, Ph.D., Niko Hänninen, M.Sc.
May 13, 2022
Keywords: Spectral diffuse optical tomography, Bayesian inverse problems, Approximation error modelling

Abstract

Diffuse optical tomography is an imaging modality where an image is obtained by reconstructing the spatial distributions of optical parameters from near-infrared optical measurement data. Typically in diffuse optical tomography, distributions of absorption and scattering parameters are reconstructed. However, if multiple wavelengths are used, concentration of light absorbing molecules can be estimated. This spectral diffuse optical tomography utilises a model that connects molecule concentrations and absorption spectra of the molecules to form the (total) absorption coefficient.

In this thesis, spectral diffuse optical tomography was investigated. A model for describing light propagation in multi-wavelength diffuse optical tomography was studied and its numerical approximation was implemented. The inverse problem of estimating the concentrations of light absorbing molecules was derived and implemented. The approach was evaluated using numerical simulations. In addition to known spectra, also uncertainties in the spectra and compensating the related errors using Bayesian approximation error modelling were studied.

In the simulations, various concentration and scattering parameter distributions were reconstructed using the approach. For comparison, a reference set of reconstructions was computed using a technique in which estimates of optical parameters were first computed, and chromophore concentrations were estimated from the optical parameters. In the simulations, the direct estimation technique was consistently found to provide more accurate reconstructions compared to the reference technique. Furthermore, the Bayesian approximation error approach was found to successfully reduce errors arising from inaccuracies in the approximated spectra.

Tiivistelmä

Diffuusi optinen tomografia on kuvantamismenetelmä, jossa kuva tuotetaan rekonstruoimalla optisten parametrien alueelliset jakautumat lähi-infrapunamittauksista. Tyypillisesti diffuusisissa optisessa tomografiassa rekonstruoidaan absorption ja sironnan jakaumat. Useita aallonpituuksia käyttämällä voidaan kuitenkin estimoida valoa absorboivien molekyylien pitoisuudet. Spektraalissa diffuusissa optisessa tomografiassa hyödynnetään mallia, jossa kokonaisabsorptiokerroin muodostetaan yhdistämällä molekyylipitoisuudet ja molekyylien absorptiospektrit.

Tässä pro gradu -tutkielmassa tarkasteltiin spektraalia diffuusia optista tomografiaa. Työssä tarkasteltiin valon etenemisen mallia usean aallonpituuden diffuusissa optisessa tomografiassa ja hyödynnettiin mallin numeerista ratkaisua. Työssä johdettiin valoa absorboivien molekyylien pitoisuuksien estimoinnin käänteisongelma, ja lähestymistapaa testattiin numeerisilla simulaatioilla. Tunnettujen spektrien lisäksi työssä tarkasteltiin myös spektrien epätarkkuuksia ja niihin liittyvien virheiden kompensoimista Bayesilaisella approksimaatiovirhemenetelmällä.

Simulaatioissa rekonstruoitiin useita pitoisuus- ja sirontaparametrijakaumia spektraalia lähestymistapaa käyttämällä. Rekonstruktiot laskettiin myös vertailumenetelmällä, jossa optisten parametrien estimaatit laskettiin ensin ja kromoforipitoisuudet estimoitiin optisista parametreistä. Simulaatioissa suora estimointi tuotti johdonmukaisesti tarkempia rekonstruktioita kuin vertailumenetelmä. Lisäksi Bayesilaisen approksimaatiovirhemenetelmän todettiin vähentävän arvioitujen spektrien epätarkkuuksista johtuvia virheitä.

Nomenclature

Abbreviations

BAE	Bayesian approximation error
CW	Continuous wave
DA	Diffusion approximation
DCE	Dynamic contrast enhanced
DOT	Diffuse optical tomography
DW	Diffusion weighted
FEM	Finite element methods
MAP	Maximum a posteriori
MRI	Magnetic resonance imaging
NIR	Near-infrared
PET	Positron emission tomography
SDIR	Spectral derivative image reconstruction
TPSF	Temporal point spread function

Symbols

χ	Characteristic function of disjoint pixels
ϵ	Approximation error
η_μ	Means of optical parameters
η_e	Mean of (measurement) noise
η_n	Mean of total errors
η_x	Means of chromophore concentrations and scattering coefficients
$\eta_{\epsilon_{\lambda_i}}$	Approximation error mean at λ_i
Γ	Exitance
Γ_μ	Covariance of optical parameters
Γ_e	Covariance of random noise
Γ_n	Covariance of total noise
Γ_x	Covariance of chromophore concentrations and scattering coefficients
$\Gamma_{\epsilon_{\lambda_i}}$	Approximation error covariance at wavelength λ_i
$\hat{\Gamma}$	Approximated covariance
$\hat{\mu}$	Estimated optical parameters
$\hat{\tau}$	Estimated scattering coefficients
$\hat{c}$	Estimated concentrations
$\hat{n}$	Outward unit boundary normal
$\hat{s}'$	Light propagation direction
$\hat{s}$	Scattering direction
$\hat{x}$	Estimated chromophore concentrations and scattering parameters
κ	Diffusion coefficient
κ^h	Discretised diffusion coefficient
λ	Wavelength
λ_{Ref}	Reference wavelength
$\mathcal{J}$	Jacobian
$\mathcal{N}$	Normal distribution
$\mathcal{U}$	Uniform distribution

$\mu'^{\lambda_i}_s$	Scattering coefficient at wavelength λ_i
μ'_s	Reduced scattering coefficient
$\mu'_{s,\mathrm{Ref}}$	Reference reduced scattering coefficient
μ	Vector containing optical parameters
μ_a	Absorption coefficient
μ_a^h	Discretised absorption coefficient
$\mu_a^{\lambda_i}$	Absorption coefficient at wavelength λ_i
μ_s	Scattering coefficient
μ_t	Light attenuation coefficient
$\mu_{a,i}$	Absorption coefficient of the i'th chromophore
ν	Frequency
Ω	Domain
ω	Angular modulation frequency of an input signal
$\partial\Omega$	Boundary
Φ	Photon density vector
ϕ	Photon density
π	Probability density
σ_1, σ_2	Standard deviations determining the inclusion size and smoothness
σ_e	Standard deviation of the noise
$\sigma_{\hat{x}_j}$	Approximated standard deviation of element j in the estimated parameter vector
c	Speed of light in a vacuum
φ	Nodal basis function
$\vec{r}$	Position
ζ	Refractive index mismatch coefficient
ζ_k	Step length
A	Forward operator
a_{μ_a}	Lower limit of a sampling interval
a_{μ_b}	Upper limit of a sampling interval
A_{c_i}	Magnitude of a c_i inclusion
B	FEM matrix
b	Scattering power
C	FEM matrix
c_i	Concentration of the i'th chromophore
$c_{i,b}$	Background concentration
D	FEM matrix
$d\Omega'$	Differential solid angle element
d_j	Position of the j'th light source
e	Random noise
F	Product of (experimental) noise Cholesky decomposition and the forward operator
g	Scattering shape parameter
g_k	Gradient
H_k	Approximation of a Hessian matrix
K	FEM matrix
L	Radiance
L_μ	Cholesky decomposition of optical parameters
L_e	Cholesky decomposition of noise

L_n	Cholesky decomposition of total error
L_x	Cholesky decomposition of the prior of the chromophore concentrations and scattering parameters
n	Total error
N_D	Domain dimension
N_e	Number of elements
N_n	Number of nodes
N_s	Sample size
P	Phase function
Q	FEM matrix
q	Source distribution on the boundary
r_1, r_2	Elements of a 2D position vector
$r_{\mathcal{N}}$	Sample from a normal distribution
S	Power of the light sources
t	Time
x	Vector containing chromophore concentrations and scattering parameters
y	Observations

Contents

1 Introduction

There has been increasing interest in utilising electromagnetic fields in biomedical optical imaging since 1990s', and thus novel techniques such as electrical impedance tomography (EIT) and diffuse optical tomography (DOT) have been developed. The interest in utilising light arises from its capability to provide information on tissue chromophores such as oxygenated and deoxygenated haemoglobin. Overall, utilising light in biomedical applications is attractive because measurement systems can be made compact and portable, and light does not pose the same hazards as other emission types such as x-rays in computed tomography (CT) and positrons in positron emission tomography (PET). DOT uses near-infrared light (NIR) to image body structure and function, and it has applications in fields such as functional cortical imaging and optical mammography [1].

In DOT, the objective is to obtain an image (a reconstruction) of the spatial distribution of light absorbing chromophores in the target. Images of the target volume are reconstructed using boundary measurement data, to quantify the spatially distributed optical properties of the medium. Light attenuation in the medium is assumed to result from both light absorption and scattering inside the target volume. Commonly, DOT images are spatial distributions of optical absorption and scattering coefficients in the target volume. These optical parameters can be used to estimate chromophore distributions when the corresponding chromophore absorption spectra are known [2].

The image reconstruction problem in DOT, where optical parameters are estimated from the light measurements, is an ill-posed inverse problem. Ill-posedness means that even small errors in measurements or modelling can cause large errors in the reconstruction. Solving the inverse problem requires solutions to the optical forward problem, in which the measurements are computed with known optical parameters and measurement setup configurations i.e. light attenuation measurements are determined from known optical parameters.

Although in many cases absorption and scattering coefficients are estimated in DOT, a lot of interest lies in reconstructing concentrations of light absorbing molecules. Estimation of chromophores is called spectral diffuse optical tomography [3]. In spectral DOT, a target volume is scanned using light at multiple wavelengths. Since absorption coefficients of chromophores are wavelength-dependent, using multiple wavelengths allows differentiating various chromophore concentrations [3].

Estimation of chromophore concentrations has been conventionally performed as a next step after optical parameters are estimated [2]. Alternatively, chromophore concentrations and scattering parameters may be directly estimated from the imaging data [4]. This approach expresses the light transport data as a function of chromophore concentrations and scattering parameters. A study has shown that utilising spectral data and models can reduce noise, improve tissue water quantification and suppress imaging artifacts when compared to the conventional method [4]. Spectral DOT commonly assumes that the chromophore absorption spectra are known. The assumption is not necessarily accurate. Utilising inaccurate absorption spectra can cause imaging errors [5].

In this thesis, the Bayesian approach to the inverse problem of spectral diffuse optical tomography is formulated. The image reconstruction problem is formulated as a minimisation problem and solved using a Gauss-Newton method. The diffusion approximation (DA) is used to model light propagation. Uncertainties in the solution are studied using Gaussian approximations for the posterior densities. Uncertainties in the chromophore spectra and their impact

on the reconstructed images are studied. Further, modelling of the these uncertainties using Bayesian approximation error modelling is proposed. The methodology is evaluated using numerical simulations.

The rest of the thesis is structured as follows. Section 2 reviews the background of spectral diffuse optical tomography by describing the optical parameters and models needed to perform spectral DOT imaging, introducing the modelling and numerical implementation used for spectral DOT simulations of this thesis and reviewing relevant clinical applications. In Section 3, a minimisation problem for solving the spectral DOT problem is formulated and the Gauss-Newton approach used for solving the minimisation problem is described. Section 4 presents the set-up and results of the spectral DOT simulations performed in this thesis. Section 5 draws conclusions of the work.

2 Diffuse optical tomography

2.1 Experimental setup

Diffuse optical tomography is performed using near-infrared (NIR) light sources and detectors that are attached to the surface of the imaged target [6]. Sources are used to introduce visible or near-infrared light in the target, and the transmitted light is measured using light sensitive detectors. In tomographic measurements, the sources and detectors are generally placed around the target to obtain data from a comprehensive set of angles and directions instead of solely on one side [1]. For example, DOT imaging of neonatal brain has been performed using a flexible headband to which the sources and detectors were attached [7].

Three types of imaging systems have been developed for DOT: continuous wave (CW) system, time-domain system and frequency domain system [1]. Examples of data types measured with different systems are presented in Figure 1. In a continuous wave imaging system, the sources either illuminate the tissue with a constant light intensity or the NIR light signal is modulated at a low frequency [1]. The signal between a specific source-detector pair is isolated from the total signal by activating the sources at separate times or by having the sources transmit the signal at different frequencies. The signal from a given light source can be isolated from the frequency-encoded signal using lock-in amplifiers or Fourier transformation.

In a time-domain system, the light emission from the NIR sources is pulsed and photon counting detectors are commonly used for signal detection. This enables measuring photon flight times and approximating the temporal point spread function (TPSF). The TPSF is the temporal distribution of photons transmitted in a light pulse and it may be used to extract the target volume optical properties [8].

A frequency-domain system consists of amplitude-modulated sources and is used for determining the reduction in signal amplitude and phase shift [1]. Compared to the CW system, the time-domain and frequency-domain systems are capable of imaging large thicknesses of tissue with a higher resolution [1]. Effective imaging of tissues below 6 cm in depth commonly requires the use of photon counting detectors and pulsed sources characteristic to a time-domain system [1]. While time-domain systems are especially sensitive as imaging systems, frequency-domain systems are more cost-effective and easier to develop.

One of the challenges faced by DOT is a high dependence on surface coupling. Surface coupling refers to differences in skin contact properties between optical sensors. For example, the firmness of optical sensor placement has a notable impact on the measurements. Therefore, a calibration routine to account for the varying surface coupling between optical sensors is required. Alternatively, a difference imaging approach to DOT can be used to cancel out errors induced by unknown surface coupling properties [9]. As opposed to absolute imaging, where a single measurement set is used to image target optical properties, difference imaging estimates the temporal change in optical parameters from data sets y_{t_1} and y_{t_2} measured at time instants t_1 and t_2.

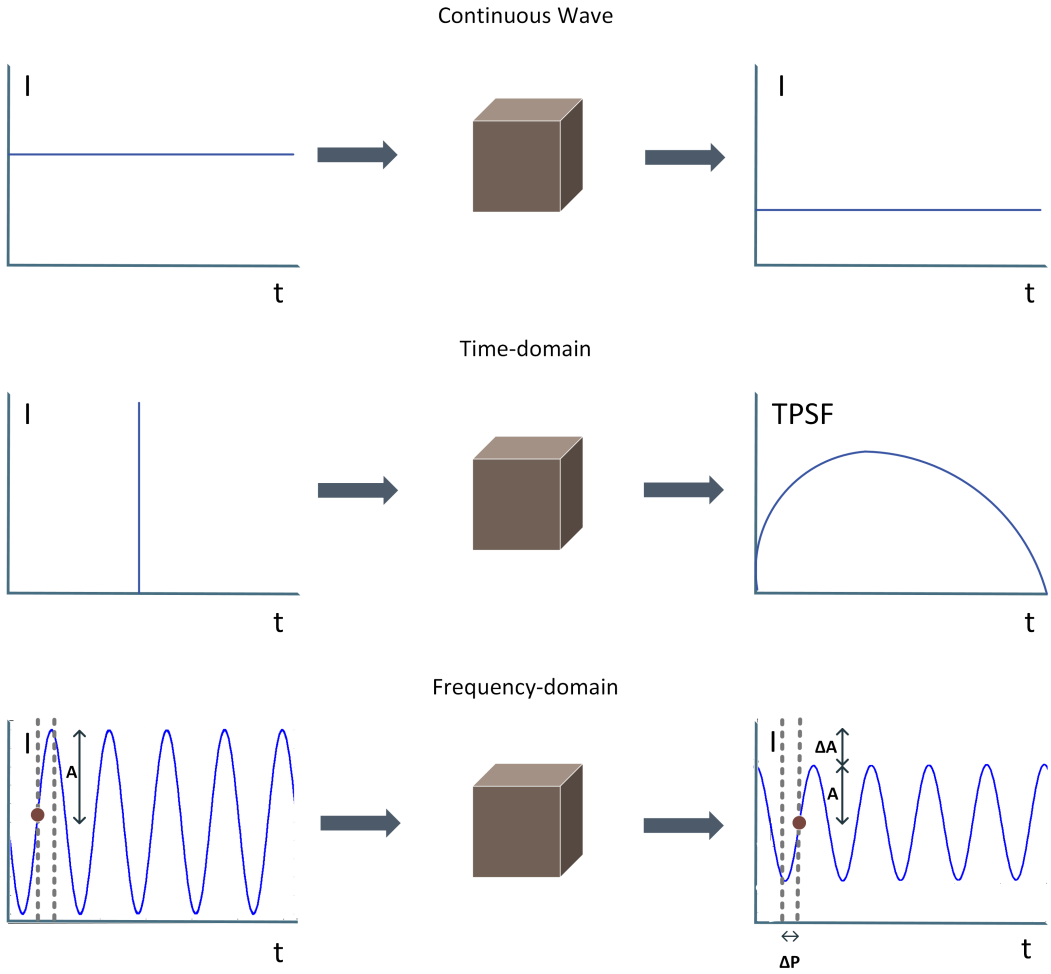

Figure 1: An illustration of data that may be obtained when a light signal passes through the target medium. A continuous wave system (top row) measures the decrease in light intensity (I) versus time (t), a time-domain system (middle row) may be used to measure the temporal point spread function (TPSF) and the frequency-domain system (bottom row) is sensitive to the change in light signal amplitude (A) and phase (P).

2.2 Forward modelling

2.2.1 Light transport modelling

The forward problem in diffuse optical tomography is to solve the measurable data when optical parameters of the object, measurement configuration and the amount of input light are given. Absorption is a light-matter interaction mechanism where electromagnetic field energy of light is converted into internal energy of the medium. In scattering, the propagation direction of light changes as a result of light interacting with the medium. Scattering has a high contribution to the total light attenuation, which makes it practical to model near-infrared light transfer through medium as a diffusive process [10, 11].

Photon transfer through a medium can be modeled with the radiative transfer equation

$$\begin{aligned}\frac{\mathrm{i}\omega}{\mathrm{c}}L(\vec{r},\hat{s}) = &-\hat{s}\cdot\nabla L(\vec{r},\hat{s}) - \mu_t L(\vec{r},\hat{s}) \\ &+ \mu_s\int_{4\pi} L(\vec{r},\hat{s}')P(\hat{s}'\cdot\hat{s})d\Omega' + S(\vec{r},\hat{s})\end{aligned} \tag{1}$$

with a boundary condition

$$L(\vec{r},\hat{s}) = \begin{cases} L_0(\vec{r},\hat{s}), & \vec{r}\in\cup_j d_j, \quad s\cdot\hat{n}<0 \\ 0, & \vec{r}\in\partial\Omega\setminus\cup_j d_j, \quad s\cdot\hat{n}<0 \end{cases} \tag{2}$$

where ω is the angular modulation frequency of the input signal, i is the imaginary unit, c is the speed of light, μ_t is the attenuation coefficient of the medium, μ_a is the absorption coefficient and μ_s is the scattering coefficient. The attenuation coefficient is the probability of light extinction in a medium through absorption or scattering and is computed as $\mu_t = \mu_a + \mu_s$. Further, $L(\vec{r},\hat{s})$ is radiance at position $\vec{r}$ towards the direction of unit direction vector $\hat{s}$ [12]. Radiance L is the spectral radiance $L_\upsilon(\vec{r},\hat{s})$ integrated over a frequency interval $[\upsilon,\ \upsilon+\Delta\upsilon]$

$$L(\vec{r},\hat{s}) = L_\upsilon(\vec{r},\hat{s})\Delta\upsilon. \tag{3}$$

Spectral radiance $L_\upsilon(\vec{r},\hat{s})$ is the energy flow through area perpendicular to the flow direction per solid angle, in a time unit and per temporal frequency. Phase function $P(\hat{s}'\cdot\hat{s})$ is a probability density function that describes the probability that light propagating towards the direction $\hat{s}'$ scatters towards unit vector $\hat{s}$, $d\Omega'$ is a differential solid angle element around direction $\hat{s}'$. Henyey-Greenstein scattering function is a phase function for isotropic materials. The three-dimensional form of the Henyey-Greenstein scattering function is

$$P(\hat{s}'\cdot\hat{s}) = \frac{1}{4\pi}\frac{1-g^2}{(1+g^2-2g\hat{s}'\cdot\hat{s})^{3/2}} \tag{4}$$

and the two-dimensional form is

$$P(\hat{s}'\cdot\hat{s}) = \frac{1}{2\pi}\frac{1-g^2}{1+g^2-2g\hat{s}'\cdot\hat{s}}. \tag{5}$$

The shape of the scattering function is determined by a scattering shape parameter g, $g\in]-1,\ 1[$ [13]. Additional sources in the medium produce energy with the power quantified by the

function $S(\vec{r},\hat{s})$ per volume element, per unit solid angle element and in a unit time instant ([S] = W/(m^{3}sr)). $L_0(\vec{r},\hat{s})$ is radiance at sources occupying positions d_j at the boundary $\partial\Omega$ and $\hat{n}$ is a normal vector of $\partial\Omega$. The sum of the four terms in the radiative transfer equation (1) describe how much different factors contribute to the rate of change in radiance. The term $-\hat{s}\cdot\nabla L(\vec{r},\hat{s})$ quantifies the energy divergence out of a volume element, the term $-\mu_t L(\vec{r},\hat{s})$ describes energy loss due to photon extinction, the term $\mu_s\int_{4\pi} L(\vec{r},\hat{s}')P(\hat{s}'\cdot\hat{s})d\Omega'$ represents the energy incident on the volume element from the surrounding space and the term $S(\vec{r},\hat{s})$ describes the energy generation from a source in the volume element. [14]

Generally in DOT, the DA of the RTE is used as the model for light propagation [6]. The DA can be obtained through approximating the radiance $L(\vec{r},\hat{s})$, phase function $P(\hat{s}'\cdot\hat{s})$ and source power $S(\vec{r},\hat{s})$ by truncating the Taylor expansions of these functions [10]. Additionally, the angular distribution of radiance $L(\vec{r},\hat{s})$ is assumed to be nearly uniformly distributed and the light sources are assumed to be isotropic. In practice, these approximations are valid in a medium where $\mu_a << \mu_s$, which is a valid assumption for most biological tissues. The frequency domain DA is

$$-\nabla\cdot\kappa(\vec{r})\nabla\phi(\vec{r},\omega)+\left[\mu_a(\vec{r})+\frac{\mathrm{i}\omega}{\mathrm{c}}\right]\phi(\vec{r},\omega)=q_0(\vec{r},\omega),\qquad \vec{r}\in\Omega \tag{6}$$

with the boundary condition

$$\phi(\vec{r},\omega)+\frac{\zeta}{2\gamma}\kappa(\vec{r})\frac{\partial\phi(\vec{r},\omega)}{\partial\hat{n}}=q(\vec{r},\omega),\qquad \vec{r}\in\partial\Omega, \tag{7}$$

where

$$\kappa(\vec{r})=\frac{1}{N_D[\mu_a(\vec{r})+\mu_s'(\vec{r})]} \tag{8}$$

is the diffusion coefficient at position $\vec{r}$, $\mu_s'=(1-g)\mu_s$ is reduced scattering coefficient, $\phi(\vec{r},\omega)$ is the photon density at angular modulation frequency ω, $q_0(\vec{r},\omega)$ is an isotropic light source inside the medium, ζ is a coefficient that accounts for the refractive index mismatch at the boundary $\partial\Omega$, $\hat{n}$ is the outward unit boundary normal, $q(\vec{r},\omega)$ is the source distribution at position $\vec{r}$ on the boundary, γ is a dimension dependent constant that has a value $\frac{1}{\pi}$ in 2D and $\frac{1}{4}$ in 3D, the domain Ω is limited by the boundary $\partial\Omega$ and N_D is the dimension of domain Ω so that $N_D=2$ for a 2D domain and $N_D=3$ for a 3D domain. Photon density is radiance integrated over angular directions

$$\phi(\vec{r},\omega)=\int_\Omega L(\vec{r},\hat{s})d\hat{s}. \tag{9}$$

The measurable quantity in DOT is the exitance Γ. Using the DA, the exitance for a light source i and a detector j can be obtained from the equation

$$\Gamma_{ij}(\vec{r},\omega)=\int -\kappa(\vec{r})\frac{\partial\phi_i(\vec{r},\omega)}{\partial\hat{n}}d\Omega\qquad r\in d_j, \tag{10}$$

where $\hat{n}$ is the outward normal of the boundary at position $\vec{r}$ and $d_j\in\partial\Omega$ are the detector locations on the boundary [15].

2.2.2 Finite element implementation

In this work, we use finite element method (FEM) to approximate the solution of the DA. A domain Ω is divided into N_e elements so that the element vertices connect at one of the N_n vertex nodes. Photon density ϕ is approximated as

$$\phi(\vec{r},\omega) \approx \sum_{j=1}^{N_n} \Phi_j(\omega)\varphi_j(\vec{r},\omega) \tag{11}$$

where φ_j are nodal basis functions of the finite element mesh and $\Phi_j(\omega)$ are photon densities in the nodes of the finite element mesh. The optical absorption, scattering and diffusion coefficients are approximated as

$$\mu_a(\vec{r}) \approx \sum_{k=1}^{N_n} (\mu_a)_k \varphi_k(\vec{r}) \tag{12}$$

$$\mu_s'(\vec{r}) \approx \sum_{k=1}^{N_n} (\mu_s')_k \varphi_k(\vec{r}) \tag{13}$$

$$\kappa(\vec{r}) \approx \sum_{k=1}^{N_n} \kappa_k \varphi_k(\vec{r}) \tag{14}$$

where φ_k are piece-wise linear nodal basis functions [15]. A nodal coefficient vector $\Phi(\omega)$ of nodal photon densities $\Phi_j(\omega)$ can be solved by solving a linear system

$$[K(\kappa) + D(\mu_a) + \frac{1}{2\zeta}B + \mathrm{i}\omega C]\Phi(\omega) = Q(\omega) \tag{15}$$

where $\Phi(\omega)$ is a vector of photon densities $\Phi_j(\omega)$. Further, K, D, B and C are sparse symmetric positive definite system matrices of the following form

$$K_{ij}(\kappa(\vec{r})) = \sum_{k=1}^{N} \kappa_k \int_\Omega \varphi_k(\vec{r},\omega)\nabla\varphi_j(\vec{r},\omega)\cdot\nabla\varphi_i(\vec{r},\omega)d\vec{r} \tag{16}$$

$$D_{ij}(\mu_a(\vec{r})) = \sum_{k=1}^{N} (\mu_a)_k \int_\Omega \varphi_k(\vec{r},\omega)\varphi_j(\vec{r},\omega)\varphi_i(\vec{r},\omega)d\vec{r} \tag{17}$$

$$C_{ij} = \frac{1}{\mathrm{c}} \int_\Omega \varphi_i(\vec{r},\omega)\varphi_j(\vec{r},\omega)d\vec{r} \tag{18}$$

$$B_{ij} = \int_{\partial\Omega} \varphi_i(\vec{r},\omega)\varphi_j(\vec{r},\omega)d\vec{r} \tag{19}$$

$$Q_i = \int_\Omega q_0(\vec{r},\omega)\varphi_i(\vec{r},\omega)d\vec{r}. \tag{20}$$

The FEM matrix equation (15) is derived in Appendix I. [16, 17]

2.3 Applications

Various applications of DOT have been studied till date. Conventionally, DOT together with correct modelling of light transport has been utilised in few applications and these studies have mostly concentrated on single-wavelength DOT and estimating absorption and scattering. In spectral DOT, approximate light attenuation models, such as linear and exponential, have typically been used. Nonetheless, also these studies indicate the potential of DOT in variety of applications.

One of the most interesting applications of DOT is brain imaging. Blood oxygenation mapping by spectral DOT can be used for tracking haemodynamic responses. A haemodynamic response is a regional oxygenation change in the brain due to oxygen consumption of neural activity. Due to its haemodynamic sensitivity, spectral DOT has been evaluated in studies as a potential functional cortical imaging technique [18]. In a functional imaging study, the neural activity from a finger tapping task was visible in a DOT reconstruction as a regional and temporal increase of optical absorbance in the motor cortex [19]. Other experiments have trialed spectral DOT in real-time monitoring of epileptic seizure generation and propagation [20], mapping the resting-state networks of the brain and mapping cortical responses to different word stimuli in set-ups where a subject hears or reads a word, imagines themselves speaking a word or is tasked with generating a verb that is associated with a given word [21]. While functional imaging is conventionally performed using positron emission tomography (PET) or functional MRI, DOT is a potential noninvasive and portable alternative to the established imaging techniques. Besides functional imaging, spectral DOT reconstructions may have diagnostic value in anatomical imaging. In one case, a cerebral haemorrhage was located in an infant brain using spectral DOT. The hemorrhage was detected because of a regional blood volume increase and an oxygenation decrease [22]. In another study, spectral DOT was successfully used to detect a perinatal stroke both with and without the assistance of MRI-guided stroke localisation [23].

In addition to imaging brain, DOT can be applied in breast tissue imaging (optical mammography). Optical mammography is a prospective diagnostic tool for detection and characterisation of breast tumors as blood volume or oxygenation maps produced in DOT imaging can reveal tumors by exploiting the increased vascularisation of a tumor and because breast tumors appear to have higher concentrations of both oxy- and deoxyhemoglobin compared to the background in a spectral DOT image [1, 24]. Spectral DOT has been demonstrated to be capable of detecting breast tumors and potentially distinguishing malignant tumors from benign ones as malignant tumors have higher concentrations of total hemoglobin and oxyhemoglobin and higher scattering than benign tumors [25]. Optical mammography could be performed to assess tissue angiogenesis and thus improve the accuracy of early cancer diagnosis [26] or to monitor the patient's response to neoadjuvant hormone therapy of breast cancer [27].

Synovial inflammation associated with arthritis causes the metabolic demand of a synovial tissue to increase and thus makes the tissue hypoxic. The hypoxia is distinguishable in a spectral DOT image and may indicate that the joint is arthritic [28]. One study concluded that DOT images could be utilised in detecting and monitoring joint diseases such as osteoporosis and osteoarthritis [29] while another demonstrated that DOT could provide additional diagnostic value in the early stages of rheumatoid arthritis [30]. Other applications of DOT include for example, small animal imaging and muscle oxygenation monitoring [31].

3 Inverse problem

3.1 Bayesian image reconstruction in diffuse optical tomography

The inverse problem of DOT is to estimate distributions of the optical parameters when input light and measured data are given. There are two methodologies to reconstruct the imaging target: absolute imaging and difference imaging. In absolute imaging, distributions of optical parameters are estimated using one set of measurement data. In difference imaging, the difference in the optical parameters between two time instants is estimated. Difference imaging reduces artefacts because the imaging errors cancel out. However, the images often have low contrast. One of the imaging artefacts is cross-talk, which is a phenomenon where characteristics of a parameter distribution appear in an image depicting another parameter e.g. deoxyhemoglobin inclusion being visible in an oxygemoglobin image or absorption inclusion appearing in the scattering coefficient reconstruction.

In both the absolute imaging method and the difference imaging method, the inverse problem is solved using methods of computational optimisation. Both of the problems are ill-posed and therefore they need to be approached in the framework of inverse problems. The approaches to solving these inverse problems are for example regularisation methods such as Tikhonov regularisation and total variation regularisation, and a Bayesian approach. In this thesis, absolute imaging is studied in the Bayesian framework.

Let us denote discrete absorption and scattering vector as

$$\mu = \begin{pmatrix} \mu_a \\ \mu_s' \end{pmatrix} \in \mathbb{R}^{2N}, \tag{21}$$

where N is the number of unknown absorption or scattering coefficients and the measurement vector as

$$y = \begin{pmatrix} \operatorname{Re}\log(\Gamma) \\ \operatorname{Im}\log(\Gamma) \end{pmatrix} \in \mathbb{R}^M \tag{22}$$

where Γ is the measured exitance (equation (10)) and M is the amount of elements in the measurement vector y. In this work, we use an observation model

$$y = A(\mu) + e \tag{23}$$

where e is random measurement noise and A is discretized forward operator which maps the optical parameters μ to observations y. [15] In the Bayesian framework, all variables y, μ and e are considered as random variables. The solution to the inverse problem is the posterior probability density $\pi(\mu|y)$ which according to the Bayes' formula is

$$\pi(\mu|y) = \frac{\pi(\mu)\pi(y|\mu)}{\pi(y)}, \tag{24}$$

where $\pi(\mu)$ is the prior density, $\pi(y|\mu)$ is the likelihood density and $\pi(y)$ is the normalization constant. Because $\pi(y)$ is constant for a given measurement, the posterior probability density $\pi(\mu|y)$ is proportional to

$$\pi(\mu|y) \propto \pi(\mu)\pi(y|\mu). \tag{25}$$

If the random variables μ and e are uncorrelated, this becomes

$$\pi(\mu|y) \propto \pi(\mu)\pi_e(y - A(\mu)), \tag{26}$$

where π_e is the probability density of the noise e. In this work, we use Gaussian models for the prior $\pi(\mu)$ and measurement noise $\pi_e(e)$

$$\mu \sim \mathcal{N}(\eta_\mu, \Gamma_\mu), \quad e \sim \mathcal{N}(\eta_e, \Gamma_e), \tag{27}$$

with means $\eta_\mu \in \mathbb{R}^{2N}$ and $\eta_e \in \mathbb{R}^M$ and covariance matrices $\Gamma_\mu \in \mathbb{R}^{2N\times 2N}$ and $\Gamma_e \in \mathbb{R}^{M\times M}$. When Gaussian probability densities are substituted into the expression (26), the posterior density $\pi(\mu|y)$ can be written in the form

$$\pi(\mu|y) \propto \exp\left\{ -\frac{1}{2}(y - A(\mu) - \eta_e)^T\Gamma_e^{-1}(y - A(\mu) - \eta_e) - \frac{1}{2}(\mu - \eta_\mu)^T\Gamma_\mu^{-1}(\mu - \eta_\mu)\right\} \tag{28}$$

In this thesis, a maximum a posteriori estimate for the parameters is computed. The maximum a posteriori estimate $\hat{\mu}$ is the maximum point of the posterior density $\pi(\mu|y)$

$$\begin{aligned}\hat{\mu} &= \arg\max_\mu \pi(\mu|y) \\ &= \arg\min_\mu\{||L_e(y - A(\mu))||^2 + ||L_\mu(\mu - \eta_\mu)||^2\}\end{aligned} \tag{29}$$

where $L_e \in \mathbb{R}^{M\times M}$ and $L_\mu \in \mathbb{R}^{2N\times 2N}$ are the Cholesky decompositions of the inverse covariance matrices $\Gamma_e^{-1} = L_e^T L_e$ and $\Gamma_\mu^{-1} = L_\mu^T L_\mu$ [32, 33]. Further, in this work it is assumed that mean of the noise is zero, that is $\eta_e = 0$. The Gaussian Ornstein-Uhlenbeck prior was used to construct matrix Γ_μ [34].

The minimisation problem (29) can be solved iteratively by using for example Gauss-Newton method, where the estimates are updated by

$$\begin{aligned}\mu^{(k+1)} =& \mu^{(k)} + \zeta_k(F'^T(\mu^{(k)})F'(\mu^{(k)}) + L_\mu^T L_\mu)^{-1} \\ & \cdot (F'^T(\mu^{(k)})(L_e y - F(\mu^{(k)})) - L_\mu^T L_\mu(\mu^{(k)} - \eta_\mu)) \\ =& \mu^{(k)} + \zeta_k H_k^{-1}(-g_k) \\ =& \mu^{(k)} + \zeta_k \Delta\mu_k\end{aligned} \tag{30}$$

where $F(\mu) = L_e A(\mu)$, ζ_k is the step length determining how much the search direction $\Delta\mu_k$ affects the estimate $\mu^{(k+1)}$, H_k is an approximation of Hessian matrix and g_k is the gradient [35]. By representing the differential function F' with the Jacobian matrix $\mathcal{J} \in \mathbb{R}^{M\times 2N}$, the update $\Delta\mu_k$ may be solved from the equation

$$\begin{aligned}H_k\Delta\mu_k &= -g_k \\ (\mathcal{J}^T\mathcal{J} + L_\mu^T L_\mu)\Delta\mu_k &= \mathcal{J}^T(L_e y - L_e A(\mu^{(k)})) - L_\mu^T L_\mu(\mu^{(k)} - \eta_\mu)\end{aligned} \tag{31}$$

where

$$\mathcal{J} = \begin{pmatrix} \frac{dF(\mu)}{d\mu_a} & \frac{dF(\mu)}{d\mu_s'}. \end{pmatrix} \tag{32}$$

3.2 Spectral diffuse optical tomography

In spectral diffuse optical tomography, the aim is to estimate concentrations of chromophores and scattering parameters from multi-wavelength measurements [4]. Chromophore absorption coefficients are dependent on the light signal wavelength which makes multi-wavelength measurements able to discern different chromophores based on their unique absorption spectra. Individual chromophores with concentration distributions c_i and wavelength-dependent absorption coefficients $\mu_{a,i}(\lambda)$ form a total absorption coefficient distribution [36]

$$\mu_a(\lambda) = \sum_{i=1}^{k} c_i \mu_{a,i}(\lambda). \tag{33}$$

Wavelength dependency of optical scattering can be modeled using Mie scattering model, where scattering coefficient at wavelength λ is

$$\mu_s'(\lambda) = \mu_{s,\mathrm{Ref}}' \Big(\frac{\lambda}{\lambda_{\mathrm{Ref}}} \Big)^{-b}, \tag{34}$$

where $\mu_{s,\mathrm{Ref}}'$ is the reference scattering coefficient at wavelength λ_{Ref} and b is the scattering power.

3.2.1 Previous studies on spectral DOT

Various approaches have been studied to solve the spectral DOT inverse problem. A case where the spectral DOT images were reconstructed using Tikhonov regularisation was compared to a case where the Euclidean norm in the Tikhonov regularisation term was replaced with a Manhattan norm (L_1 regularisation) [37]. The L_1 regularisation term is non-differentiable and to solve this issue, three alternative reconstruction algorithms suited for L_1 regularised estimation were introduced. Spectral DOT imaging using L_1 regularisation instead of Tikhonov regularisation was found to reduce cross-talk while maintaining a consistent image contrast. Another novel regularisation alternative was introduced in a study where spectral reconstruction was performed using a method where Tikhonov weights were incorporated into the Jacobian matrix whereas conventionally the weights were accounted for separately from the Jacobian [38]. The results showed that combining Tikhonov weights with the Jacobian could reduce cross-talk.

Magnetic resonance imaging (MRI) guided DOT can have a higher spatial accuracy compared to conventional DOT [39]. In an *in vivo* study, prior data from dynamic contrast enhanced (DCE) and diffusion weighted (DW) MRI images were used to construct regularisation matrices for the spectral DOT minimization problem. Including the DCE and DW prior data into spectral DOT reconstruction reduced absolute bias errors of the estimated total hemoglobin and water concentrations in a tumor. Other studies have shown that incorporating MRI or x-ray prior data into the reconstruction process could improve the spatial resolution of the images and make the localisation of inclusions more accurate [40, 41]. Including a prior has been shown to make the reconstruction characterise the true phantom composition more accurately [42, 43].

In another study, modifications to the observation model and prior data enabled estimation of chromophore volume fractions alongside the chromophore concentrations [44]. The *in vivo* clinical experiments showed that tumors were distinct in both 1000 nm and 6000 nm diameter

particle volume fraction images and that a malignant tumor could be told apart from a benign tumor as it had a higher volume fraction than the benign tumor. Furthermore, it has been proposed that spectral data could be utilised to minimise coupling effects of optical fibres [45, 46].

In [47], the data subset algorithm was utilized in spectral DOT to resolve memory capacity issues due to the large size of 3D measurement data. The algorithm divided the measurement data set into slices and identified the three slices with the highest least squares norms of the difference between measured data and approximated model data. The three selected slices were assumed to have the largest effect on the reconstructions and were used in the reconstruction process instead of the complete data set. Images reconstructed using the data subset algorithm and images reconstructed using the complete data set were found to be qualitatively and quantitatively comparable while the data subset algorithm utilized memory more efficiently.

3.2.2 Wavelength selection

Reconstruction accuracy can be enhanced by imaging the target with an optimal set of wavelengths [3, 48]. The wavelengths should be selected to maximise parameter distinguishability and minimise cross-talk.

A criteria for selecting the optimal wavelengths was obtained by deriving a residual norm from the non-uniqueness condition of the spectral DOT inverse problem to quantify the uniqueness of the inverse problem and consequently the parameter distinguishability [3]. The optimal wavelengths were chosen so that they maximise the inverse problem solution uniqueness by maximising the residual norm.

A second criteria aimed to determine that each chromophore concentration contributed equally to the measurement data [3]. It was shown that the measurement data dependency on a single parameter was proportional to the smoothness of the singular value distribution of a matrix that contained the absorption coefficients of individual chromophores for all applied wavelengths. As a result, the condition number of the absorption coefficient matrix quantified the singular value distribution smoothness. Selecting wavelengths that minimised the condition number guided the measurements towards being equally dependent on all chromophores.

A third criterion was formulated under the objective that the selected wavelengths should enable the accurate estimation of chromophore concentrations even when the absorption spectra used in the reconstruction were inaccurate [5]. An approximation of error due to spectral inaccuracy in chromophore concentration distributions was defined as a function of absorption coefficients and approximated absorption coefficient errors. The optimal wavelengths were selected so that they minimized the norm of the approximated chromophore concentration error vector.

Simulations have shown that applying wavelength optimization to spectral DOT provided an equally good image quality and reduced cross-talk compared to when a large number of wavelengths was sampled from the full spectrum (650 to 930 nm) [49]. The results suggested that spectral DOT images could be reconstructed with the accuracy of full spectrum measurements while maintaining the computational efficiency of using small wavelength sets.

3.2.3 Bayesian approach to spectral DOT

In this work we formulate and solve the inverse problem of spectral DOT in a Bayesian framework. Relation between chromophore concentrations and absorption and scattering parameters

is modelled using equations (33) and (34). Using the notation

$$x = \begin{pmatrix} c_1 \\ c_2 \\ c_3 \\ \mu'_{s,\mathrm{Ref}} \\ b \end{pmatrix} \tag{35}$$

to represent the concentrations and scattering parameters, the observation model becomes

$$y = A(x) + e. \tag{36}$$

If the observations y are known and the goal is to estimate the parameter x, we can follow the similar formulation of the inverse problem in a Bayesian framework as in the case of a single-wavelength DOT presented in Section 3.1. As a result, the MAP estimate for determining chromophore concentrations and scattering can be solved by minimising

$$\hat{x} = \arg\min_x \{||L_e(y - A(x))||^2 + ||L_x(x - \eta_x)||^2\}. \tag{37}$$

where $L_x \in \mathbb{R}^{5N \times 5N}$ is the Cholesky decomposition of the inverse prior covariance matrix and η_x is the expected value of x. The Gauss-Newton update for solving $\hat{x}$ is

$$\begin{aligned} x^{(k+1)} &= x^{(k)} + \zeta_k (F'^T(x^{(k)})F'(x^{(k)}) + L_x^T L_x)^{-1} \\ &\quad \cdot (F'^T(x^{(k)})(L_e y - F(x^{(k)})) - L_x^T L_x (x^{(k)} - \eta_x)) \\ &= x^{(k)} + \zeta_k H_k^{-1}(-g_k) \\ &= x^{(k)} + \zeta_k \Delta x_k \end{aligned} \tag{38}$$

with the notation $F(x) = L_e A(x)$. The Jacobian representation of function F' yields the equation

$$\begin{aligned} H_k \Delta x_k &= -g_k \\ (\mathcal{J}^T \mathcal{J} + L_x^T L_x)\Delta x_k &= \mathcal{J}^T (L_e y - L_e A(x^{(k)})) - L_x^T L_x (x^{(k)} - \eta_x). \end{aligned} \tag{39}$$

Derivation of the Jacobian matrix $\mathcal{J}$ is presented in Appendix II.

3.3 Bayesian approximation error modelling

In most of the previous studies, the absorption spectra of the chromophores have been assumed to be known. This however, is not necessary a valid assumption. In this thesis, we consider the modeling errors caused by uncertainties in the absorption spectra.

Bayesian approximation error (BAE) approach can be used to correct errors caused by inaccuracies in the observation model. An observation model

$$y = \tilde{A}(x, \tilde{\mu}_{a,i}) + \epsilon + e \tag{40}$$

expands the model (36) to include the approximation error

$$\epsilon = A(x, \mu_{a,i}) - \tilde{A}(x, \tilde{\mu}_{a,i}), \tag{41}$$

between forward solution $A(x, \mu_{a,i})$ when the true absorption spectra is used, and solution $\tilde{A}(x, \tilde{\mu}_{a,i})$ when the absorption spectra is fixed to some (possibly inaccurate) value. Similarly as earlier, let us model unknown parameters and noise as Gaussian distributed. Let us denote total error as

$$n = \epsilon + e. \tag{42}$$

By modeling the approximation error as a Gaussian distributed random variable with expected value of η_ϵ and covariance Γ_ϵ and ignoring the mutual dependence of the approximation errors and unknowns, the total error n is Gaussian distributed with expected value η_n and covariance Γ_n defined as

$$\eta_n = \eta_\epsilon + \eta_e \tag{43}$$
$$\Gamma_n = \Gamma_\epsilon + \Gamma_e. \tag{44}$$

With approximation error model, the MAP estimate can be solved from a minimisation problem

$$\hat{x} = \arg\min_x \{||L_n(y - \tilde{A}(x, \tilde{\mu}_{a,i}) - \eta_n)||^2 + ||L_x(x - \eta_x)||^2\} \tag{45}$$

where $L_n^T L_n = \Gamma_n^{-1}$. [50, 51]

The approximation error mean η_ϵ and covariance Γ_ϵ can be determined by sampling as follows. N_s samples of approximation error realizations $\{\epsilon^{(1)} \dots \epsilon^{(N_s)}\}$ can be generated. Each realization $\epsilon^{(l)}$ is computed as

$$\epsilon^{(l)} = A^{(l)}(x, \mu_{a,i}) - \tilde{A}^{(l)}(x, \tilde{\mu}_{a,i}) \tag{46}$$

$$\epsilon = Y^* - Y \tag{47}$$

where $\tilde{A}^{(l)}(x, \tilde{\mu}_{a,i})$ is optical measurements computed with fixed chromophore absorption coefficients and $A^{(l)}(x, \mu_{a,i})$ is simulated measurements with chromophore absorption coefficients drawn from a uniform distribution $\mathcal{U}(a_{\mu_a}, b_{\mu_a})$. The approximation error mean η_ϵ and covariance Γ_ϵ can be approximated from these error samples as

$$\eta_\epsilon = \frac{1}{N_s} \sum_{l=1}^{N_s} \epsilon^{(l)} \tag{48}$$

$$\Gamma_\epsilon = \frac{1}{N_s - 1} \sum_{l=1}^{N_s} \left(\epsilon^{(l)} - \eta_\epsilon\right)\left(\epsilon^{(l)} - \eta_\epsilon\right)^T \tag{49}$$

The simulation of the approximation error statistics can be time consuming. However, it can be done off-line before the experiments and can be utilised as long as it can be considered valid for the setup.

3.4 Credibility intervals

In order to assess the reliability of the estimates, the posterior distribution is approximated locally by a Gaussian distribution. For a Gaussian distribution, the true value of x_j is within the interval $[\hat{x}_j - 3\sigma_{\hat{x}_j},\ \hat{x}_j + 3\sigma_{\hat{x}_j}]$ with a probability of 99.7%, which is chosen to be the credibility interval utilized in this work.

By approximating the forward model A using second order Taylor series, the posterior distribution can be approximated

$$\pi_{x|y}(x|y) \sim \mathcal{N}(\hat{\eta}, \hat{\Gamma}), \tag{50}$$

where covariance matrix $\hat{\Gamma}$ is

$$\hat{\Gamma} = (J(\hat{x})^T \Gamma_e^{-1} J(\hat{x}) + \Gamma_x^{-1})^{-1}, \tag{51}$$

and $\hat{x}$ is the MAP estimate. The standard deviation $\sigma_{\hat{x}_j}$ is the square root of the j'th diagonal element in the approximated covariance matrix $\hat{\Gamma}$ [33]

$$\sigma_{\hat{x}_j} = \sqrt{\hat{\Gamma}(j,j)}. \tag{52}$$

Table 1: Background values for oxygenated blood concentration c_1, deoxygenated blood concentration c_2, fat concentration c_3, reference scattering coefficient $\mu'_{s,Ref}$ and scattering power b, Gaussian function inclusion amplitudes A and standard deviations σ_1 and σ_2 of each parameter.

	c_1	c_2	c_3	$\mu_{s,\mathrm{Ref}}$	b
background	0.007	0.006	0.03	1	0.25
A	0.06	0.06		1	4
σ_1, σ_2	4	4		3	7

4 Simulations

4.1 Data Simulation

Spatial distributions of three chromophores that appear in human body tissue were simulated. The selected chromophores were oxygenated blood, deoxygenated blood and fat. Distributions of oxygenated blood concentration c_1, deoxygenated blood concentration c_2, fat concentration c_3, reference scattering coefficient $\mu'_{s,\mathrm{Ref}}$ and scattering power b were generated in a circular finite element mesh with 2251 nodes, 4350 two-dimensional triangle elements, domain with a radius of 25mm, and the optical parameters were presented using a piece-wise linear basis. The domain was encircled by 16 sources and 16 detector optodes, modeled as Gaussian surface patches with a 2 mm width, located at equi-spaced angular intervals on the boundary. Each of the c_1, c_2, $\mu'_{s,\mathrm{Ref}}$ and b distributions contained a circular Gaussian inclusion. The amplitude of the Gaussian inclusion was adjusted to control the optical parameter values. The size of the inclusion was controlled by adjusting the standard deviation of the Gaussian distribution. The background optical parameters and amplitude and standard deviation used to create the inclusions are given in Table 1. The c_3 distribution contained no inclusion and was solely determined by the background fat concentration $c_{3,b}$ so that at any given coordinate (r_1, r_2) the fat concentration was $c_3(r_1, r_2) = c_{3,b}$. Next, absorption coefficients μ_a and scattering coefficients μ'_s at wavelengths 700, 800 and 900 nm were determined using equations (33) and (34). The chromophore absorption coefficients at each wavelength are given in Table 2 [32]. The reference wavelength λ_{Ref} in equation (34) was set to 700 nm. The frequency domain DOT data y was generated from the μ_a and the μ'_s distributions using FEM with Toast++ software forward solver [16]. Finally, random noise with zero mean and standard deviation σ_e was added to the data. In the simulations, σ_e was either 10%, 1%, 0.1% or 0.01% of the noiseless signal, added separately for each measurement data element

$$y_i = y_{i,0} + \sigma_e r_{\mathcal{N}} |y_{i,0}|, \tag{53}$$

where $y_{i,0}$ is the i'th element of vector y without random noise and $r_{\mathcal{N}} \sim \mathcal{N}(0, 1)$.

4.2 Image reconstruction

The parameters c_1, c_2, c_3, $\mu'_{s,\mathrm{Ref}}$ and b were estimated from the observation data y using the Gauss-Newton method (38). To avoid committing the inverse crime, the images were reconstructed in a different mesh than the mesh used for data generation. The inverse problem was solved in a mesh that consisted of 1933 nodes and 3726 elements.

Table 2: Chromophore absorption coefficients for oxygenated blood $\mu_{a,1}$ (mm^{-1}), deoxygenated blood $\mu_{a,2}$ (mm^{-1}) and fat μ_{a3} (mm^{-1}) at wavelengths 700, 800 and 900 nm.

	$\mu_{a,1}$	$\mu_{a,2}$	$\mu_{a,3}$
700 nm	0.9871	0.1713	0.070
800 nm	0.4496	0.4632	0.075
900 nm	0.4754	0.7155	0.080

Gaussian Ornstein-Uhlenbeck prior was used to construct covariance matrix Γ_μ [34]. The mean of the prior distribution of each parameter was set to be the background value of the corresponding parameter. The prior standard deviation of parameters c_1 and c_2 was

$$\sigma_{c_i} = \frac{1}{3}(\max(c_i) - \text{mode}(c_i)), \tag{54}$$

$i \in \{1, 2\}$, and likewise for scattering parameters $\mu'_{s,\text{Ref}}$ and b. The prior standard deviation of c_3 was selected to be 0.001 and the prior characteristic length was 8 mm. The measurement error statistics were assumed to be known and modeled as explained in Section 4.1

Four different test problems were studied where a single setting was varied:

1. background oxygenated blood concentration was varied $c_{1,b} = 0.001, 0.01, 0.04$
2. noise level was varied $\sigma_e = 10\%, 1\%, 0.1\%, 0.01\%$
3. the position of the inclusion in c_1 distribution was varied
4. the number of inclusions in c_1 distribution was varied

In addition to visual inspection, the reconstructions were compared by calculating the relative errors of the concentrations and the scattering parameters. The relative errors (RE) of the concentrations were computed as

$$RE = \frac{||c_i - \hat{c}_{i,\text{FWD}}||}{||c_i||} \cdot 100\%, \quad i \in \{1, 2, 3\} \tag{55}$$

where c_i is a simulated distribution of chromophore concentration and $\hat{c}_{i,\text{FWD}}$ is an estimated concentration distribution interpolated into the forward mesh. The relative error was computed the same way for scattering parameters $\mu'_{s,\text{Ref}}$ and b.

4.2.1 Comparison to a two-step approach

The reconstructions were compared against reconstructions obtained using a two-step reconstruction method. In the two-step approach, the optical parameters μ_a and μ'_s were estimated as presented in Section 3.1. The prior means of μ_a and μ'_s were selected to be the respective background true values of μ_a and μ'_s. The prior standard deviations were computed similarly as the prior standard deviations for concentrations in equation (54). The additive noise was modelled similarly as in the direct approach. After the optical parameters were estimated at each wavelength, the chromophore concentrations and scattering parameters were estimated from the absorption and scattering coefficients. For the chromophore concentrations, an observation model

$$\begin{pmatrix} \mu_a^{\lambda_1} \\ \mu_a^{\lambda_2} \\ \mu_a^{\lambda_3} \end{pmatrix} = \begin{pmatrix} 0.9781I & 0.1713I & 0.0700I \\ 0.4496I & 0.4632I & 0.0750I \\ 0.4754I & 0.7155I & 0.0800I \end{pmatrix} \begin{pmatrix} c_1 \\ c_2 \\ c_3 \end{pmatrix} \tag{56}$$
$$\Leftrightarrow \mu_a = H_1 c,$$

where $\mu_a^{\lambda_1}$, $\mu_a^{\lambda_2}$ and $\mu_a^{\lambda_3}$ are the Gauss-Newton estimates of the absorption coefficients with wavelengths $\lambda_1 = 700$ nm, $\lambda_2 = 800$ nm and $\lambda_3 = 900$ nm, was used. Similarly, for the scattering parameters an observation model

$$\begin{pmatrix} \ln(\mu_s'^{\lambda_1}) \\ \ln(\mu_s'^{\lambda_2}) \\ \ln(\mu_s'^{\lambda_3}) \end{pmatrix} = \begin{pmatrix} I & -\ln\left(\frac{700}{700}\right)I \\ I & -\ln\left(\frac{800}{700}\right)I \\ I & -\ln\left(\frac{900}{700}\right)I \end{pmatrix} \begin{pmatrix} \ln(\mu'_{s,\mathrm{Ref}}) \\ b \end{pmatrix} \tag{57}$$
$$\Leftrightarrow \mu'_{s,\ln} = H_2 \tau,$$

where $\ln(\mu_s'^{\lambda_1})$, $\ln(\mu_s'^{\lambda_2})$ and $\ln(\mu_s'^{\lambda_3})$ are the Gauss-Newton estimates of the scattering coefficients, was used. A logarithm of the exponent of scattering power was used to make the model linear. These observation models were used to estimate the parameters c_1, c_2, c_3, $\mu'_{s,\mathrm{Ref}}$ and b from the optical parameters μ_a and μ'_s by least squares estimation. The two-step estimates of chromophore concentrations and scattering parameters were computed by least squares estimation

$$\hat{c} = (H_1^T H_1)^{-1} H_1^T \mu_a \tag{58}$$
$$\hat{\tau} = (H_2^T H_2)^{-1} H_2^T \mu'_{s,\ln}. \tag{59}$$

where μ_a is a vector of parameters $\mu_a^{\lambda_i}$, $\imath \in \{1, 2, 3\}$, and $\mu'_{s,\ln}$ contains the parameters $\ln(\mu_s'^{\lambda_i})$.

4.3 Absorption spectra uncertainties and approximation error modelling

The inverse problem was studied in situations where there were uncertainties in the absorption spectra of the chromophores. Specifically, two test problems where approximation error was present in the reconstructions were studied. In the first study, only one of the parameters contained uncertainties, and in the second, approximation error affected all three concentrations.

In order to obtain the BAE statistics, a set of approximation error realizations ϵ_{λ_2} was generated using equation (47) so that each data set $\tilde{A}^{(l)}(x, \tilde{\mu}_{a,i})$ of exitance values (10) was computed using uniformly sampled chromophore absorption coefficients $\tilde{\mu}_{a,i} \sim \mathcal{U}(a_{\mu_a}, b_{\mu_a})$, where

$$a_{\mu_a} = 0.5\mu_{a,i}(\lambda) \tag{60}$$
$$b_{\mu_a} = 1.5\mu_{a,i}(\lambda) \tag{61}$$

and $\mu_{a,i}$ is the absorption coefficient for 800 nm wavelength light (Table 2). Absorption coefficients for 700 nm and 900 nm wavelengths were fixed to the accurate values, as presented in

Table 2. Another set ϵ_{123} was created by sampling all nine chromophore absorption coefficients from uniform distributions, which were defined similarly as in Equations (60) and (61) for all three absorption coefficients $\mu_{a,1}$, $\mu_{a,2}$ and $\mu_{a,3}$. The sample size N_s was selected to be 10000.

The sets ϵ_2 and ϵ_{123} were used to generate approximation error statistics $(\eta_{\epsilon_{\lambda_1}}, \Gamma_{\epsilon_{\lambda_1}})$ and $(\eta_{\epsilon_{\lambda_{123}}}, \Gamma_{\epsilon_{\lambda_{123}}})$ as explained in the Section 3.3.. These statistics were utilized in the minimisation problem with BAE approach separately (equation (45)). The inverse problem was solved in two test cases:

1. the c_1 absorption coefficient at 800 nm was 50% higher than the corresponding value used in solving the inverse problem

2. all three absorption coefficients at 800 nm were 50% higher than the corresponding values used in solving the inverse problem.

4.4 Results

4.4.1 Varying background oxygenated blood concentration

Reconstructed chromophore concentrations and scattering parameters of the study where the background oxygenated blood concentration was varied are shown in Figure 2. In the figure, reconstructions obtained using the proposed direct approach, where the concentrations were estimated directly from the data, are shown, and they are compared with reconstructions obtained with the two-step approach. Further, the relative errors of the estimates obtained using the direct approach are given in Table 3. The results show that increasing the background value of oxygenated blood concentration decreased the cross-talk in the $\mu'_{s,\mathrm{Ref}}$ and c_3 reconstructions. We expect that the cross-talk is mostly caused by large difference between background and inclusion values. This is supported by a study shown in Appendix III where it was seen that adjustments that reduce the difference between the minimum and maximum values of the true concentration distributions in general appear to decrease cross-talk.

When comparing the direct approach to the two-stage approach, it can be seen that generally, the proposed single-stage approach provides better quality reconstructions. This is especially evident in situations where the concentration difference between an inclusion and the background was large.

Figure 3 shows cross-sectional graphs of the true values and direct estimates from Figure 2 with credibility intervals to evaluate the accuracy of the estimates. The estimates were within the credibility interval in nearly every case, which suggests that the estimates are reliable.

4.4.2 Varying noise

Figure 4 shows direct and two-step reconstructions of the chromophore concentrations and scattering parameters with a varying noise level σ_e. The relative errors of the estimates obtained using the direct approach are given in Table 3. As it can be seen, the reconstruction accuracy is the highest around noise level $\sigma_e = 1\%$. A higher noise level caused inclusions to appear reduced, while a lower noise level created an artefact that showed dispersed objects across the target volume. It can be expected that on a high noise level (10%), the reconstructed inclusions were less distinguishable because the measurement data becomes more corrupted by the noise. On low noise levels (0.1% and 0.01%) the inclusions were difficult to distinguish because modelling errors start to have a more significant effect.

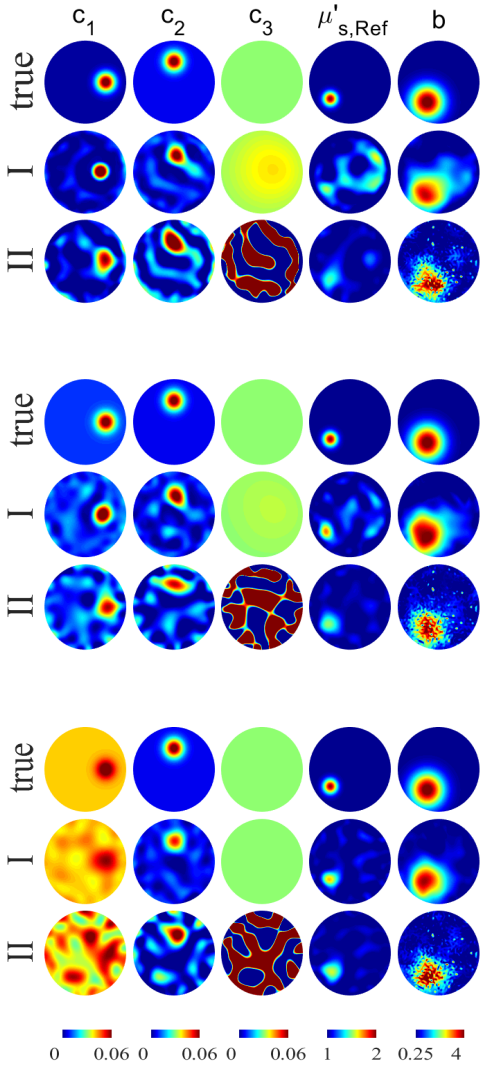

Figure 2: Varying background values of distribution c_1. Simulated distributions (true) of oxygenated blood concentration c_1 (1st column), deoxygenated blood concentration c_2 (2nd column), fat concentration c_3 (3rd column), reference scattering coefficient $\mu'_{s,Ref}$ (4th column) and scattering power b (5th column) followed by direct estimation reconstructions (I) and two-step reconstructions (II) when background oxygenated blood concentration $c_{1,b}$ is varied. In the top three rows, background value of oxygenated blood concentration was 0.001, in the next three rows 0.01 and in the last three rows 0.04.

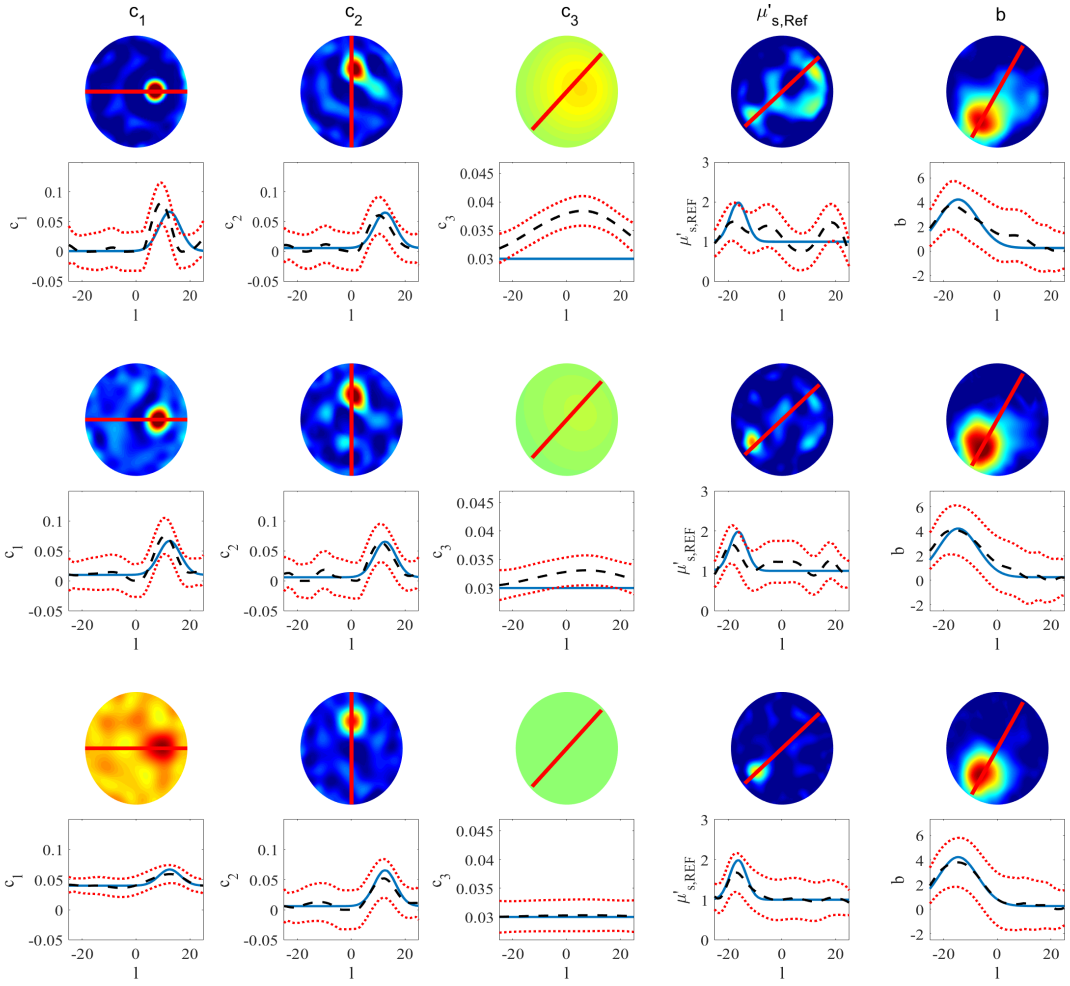

Figure 3: Varying background values of distribution c_1. Direct estimation reconstructions and cross-sectional graphs of oxygenated blood concentration c_1 (1st column), deoxygenated blood concentration c_2 (2nd column), fat concentration c_3 (3rd column), reference scattering coefficient $\mu'_{s,Ref}$ (4th column) and scattering power b (5th column) when background oxygenated blood concentration $c_{1,b}$ is varied. In the top three rows, background value of oxygenated blood concentration was 0.001, in the next three rows 0.01 and in the last three rows 0.04. The cross-sectional graphs display the true values as blue lines, estimated values as dashed lines and the credibility interval as red dotted lines.

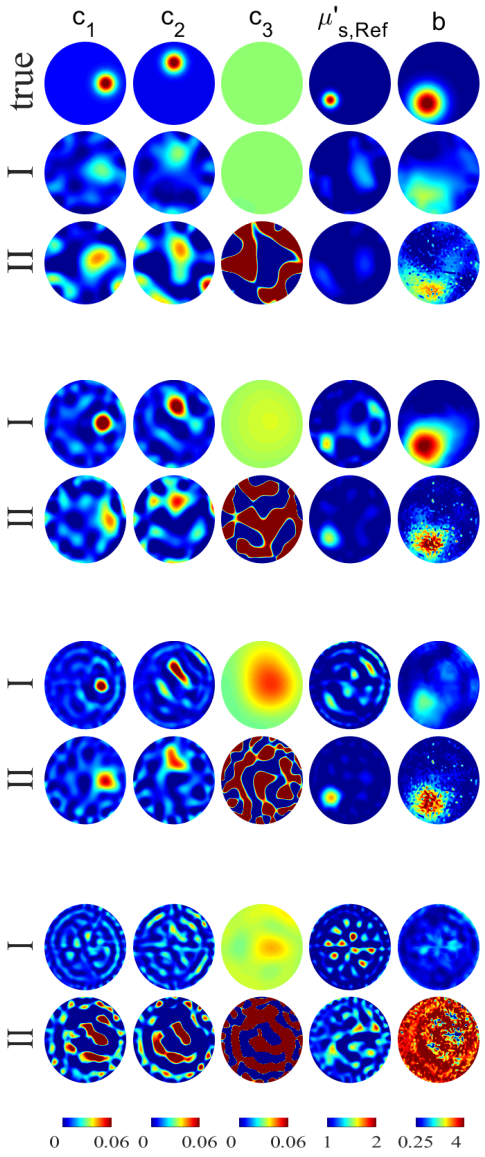

Figure 4: Varying noise level. Simulated distributions (true) of oxygenated blood concentration c_1 (1st column), deoxygenated blood concentration c_2 (2nd column), fat concentration c_3 (3rd column), reference scattering coefficient $\mu'_{s,Ref}$ (4th column) and scattering power b (5th column) followed by direct estimation reconstructions (I) and two-step reconstructions (II) when noise level is varied. In the second and the third row, noise level was 10%, in the next two rows 1%, then 0.1% for the third pair of rows, and 0.01% in the last three rows.

Table 3: Relative errors RE (%) of estimated chromophore concentrations and scattering parameters, when concentration $c_{1,b}$, noise level σ_e, position of inclusions in c_1 distribution and number of inclusions in c_1 distribution is varied. The parameter c_1 is oxygenated blood concentration, c_2 is deoxygenated blood concentration, c_3 is fat concentration, $\mu'_{s,Ref}$ is reference scattering coefficient, b is scattering power and (r_1, r_2) are the coordinates of the c_1 inclusion center.

	RE_{c_1} (%)	RE_{c_2} (%)	RE_{c_3} (%)	$\mathrm{RE}_{\mu'_{s,\mathrm{Ref}}}$ (%)	RE_b (%)
$c_{1,b} = 0.001$	84	57	17	19	36
$c_{1,b} = 0.01$	36	49	6.3	12	33
$c_{1,b} = 0.04$	5.1	31	0.67	6.4	16
$\sigma_e = 10\%$	51	53	0.13	16	48
$\sigma_e = 1\%$	54	60	10	15	36
$\sigma_e = 0.1\%$	64	87	27	21	53
$\sigma_e = 0.01\%$	81	95	15	28	84
$(r_1, r_2) = (12.5, 0)$	50	55	8.4	14	39
$(r_1, r_2) = (-18, 7)$	62	61	8.7	15	40
$(r_1, r_2) = (0, 0)$	41	63	9.8	14	40
#inclusions = 1	59	52	10	14	36
#inclusions = 2	64	61	16	21	50
#inclusions = 3	48	85	21	30	64

The two-step reconstructions portrayed the inclusions with lower accuracy and displayed dispersion artefacts and reduction in inclusion magnitude. These effects were similar to the effects seen in the directly estimated reconstructions.

Figure 5 shows the cross-sectional graphs of the true values, direct estimates and credibility intervals of the noise level variation simulations. The estimates mostly fall within the credibility interval when the noise level is in the $0.1\% - 10\%$ range, while the dispersion artefact impairs the reliability of the estimates with 0.01% noise level.

4.4.3 Varying location of an inclusion

In Figure 6, direct and two-step reconstructions of the chromophore concentrations and scattering parameters are shown while the position of the oxygenated blood inclusion was varied. Further, the relative errors of the estimates obtained using the single-step approach are given in Table 3. Especially in the case of two-step reconstruction, the reconstructed inclusion was depicted with lower accuracy in the center of the target volume that is further away from the optical probes. The direct method retained its accuracy more consistently regardless of the inclusion position when compared to the two-step method. The phenomenon where the inclusions in the oxygenated blood distribution are reconstructed more accurately near the sources and detectors (near the boundary) is typical in DOT measurements.

Figure 7 displays cross-sectional graphs of the true values, direct estimates and credibility intervals when the position of the oxygenated blood inclusion was varied. The estimates are shown to be within the credibility interval, which suggests that the estimates are reliable.

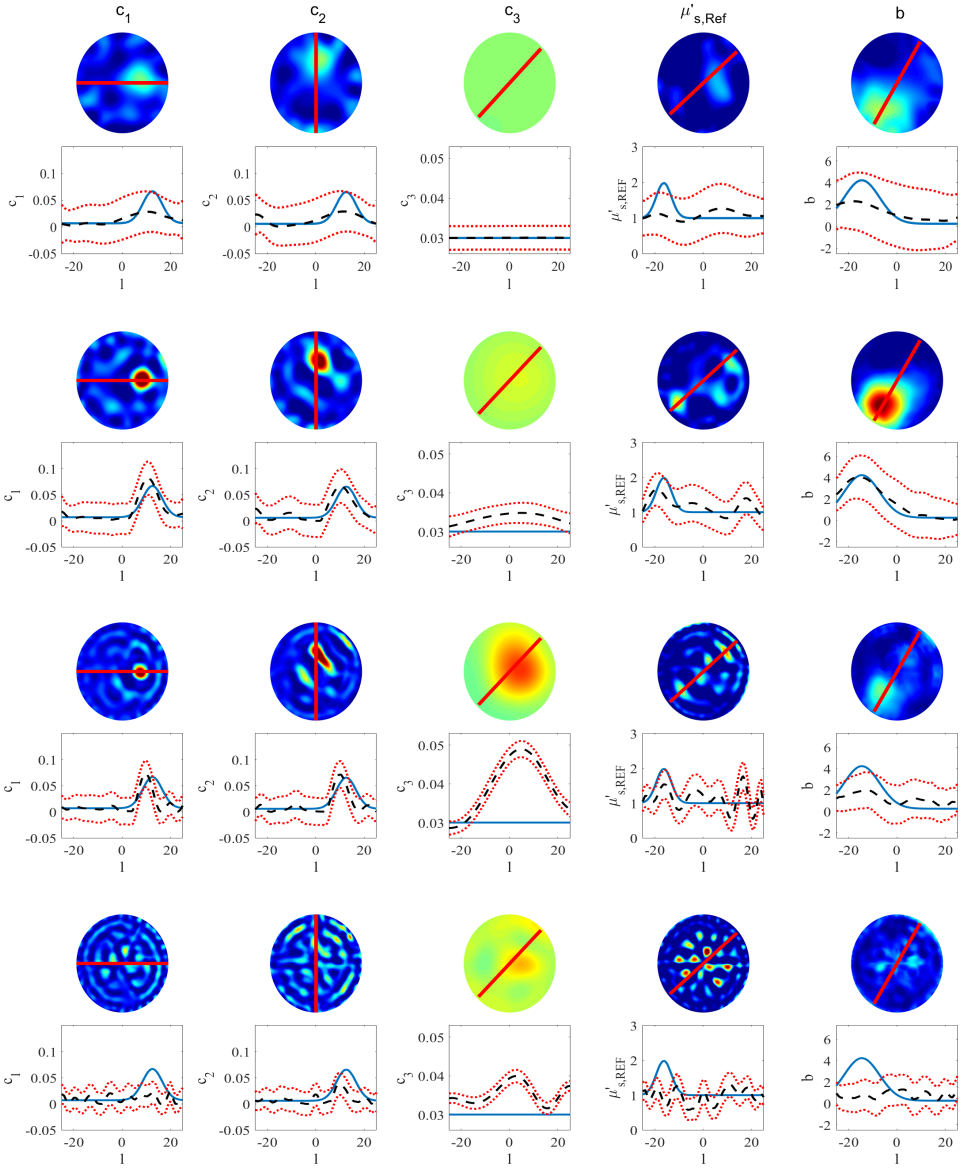

Figure 5: Varying noise level. Direct estimation reconstructions and cross-sectional graphs of oxygenated blood concentration c_1 (1st column), deoxygenated blood concentration c_2 (2nd column), fat concentration c_3 (3rd column), reference scattering coefficient $\mu'_{s,Ref}$ (4th column) and scattering power b (5th column) when noise level is varied. In the second and the third row, noise level was 10%, in the next two rows 1%, then 0.1% for the third pair of rows, and 0.01% in the last three rows. The cross-sectional graphs display the true values as blue lines, estimated values as dashed lines and the credibility interval as red dotted lines.

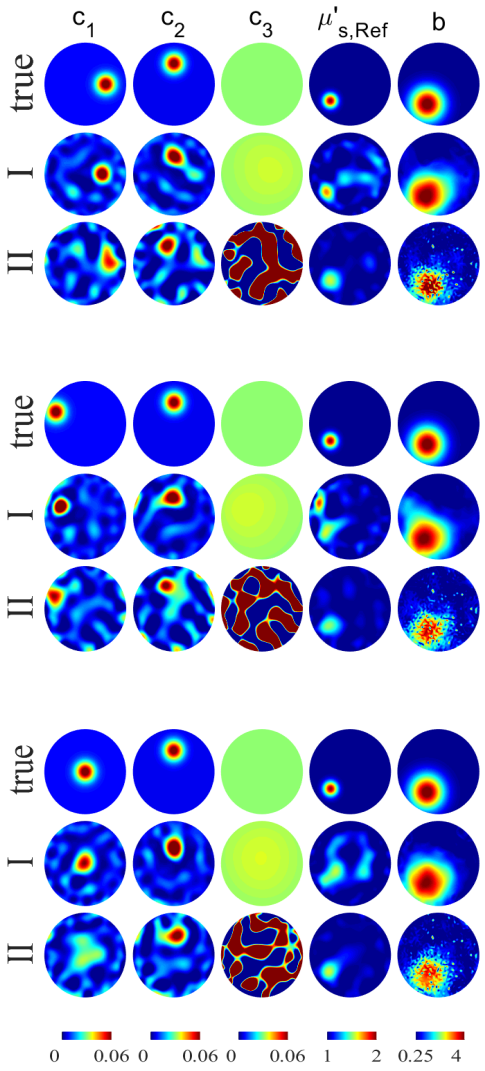

Figure 6: Varying inclusion position. Simulated distributions (true) of oxygenated blood concentration c_1 (1st column), deoxygenated blood concentration c_2 (2nd column), fat concentration c_3 (3rd column), reference scattering coefficient $\mu'_{s,Ref}$ (4th column) and scattering power b (5th column) followed by direct estimation reconstructions (I) and two-step reconstructions (II) when background c_1 inclusion position is varied.

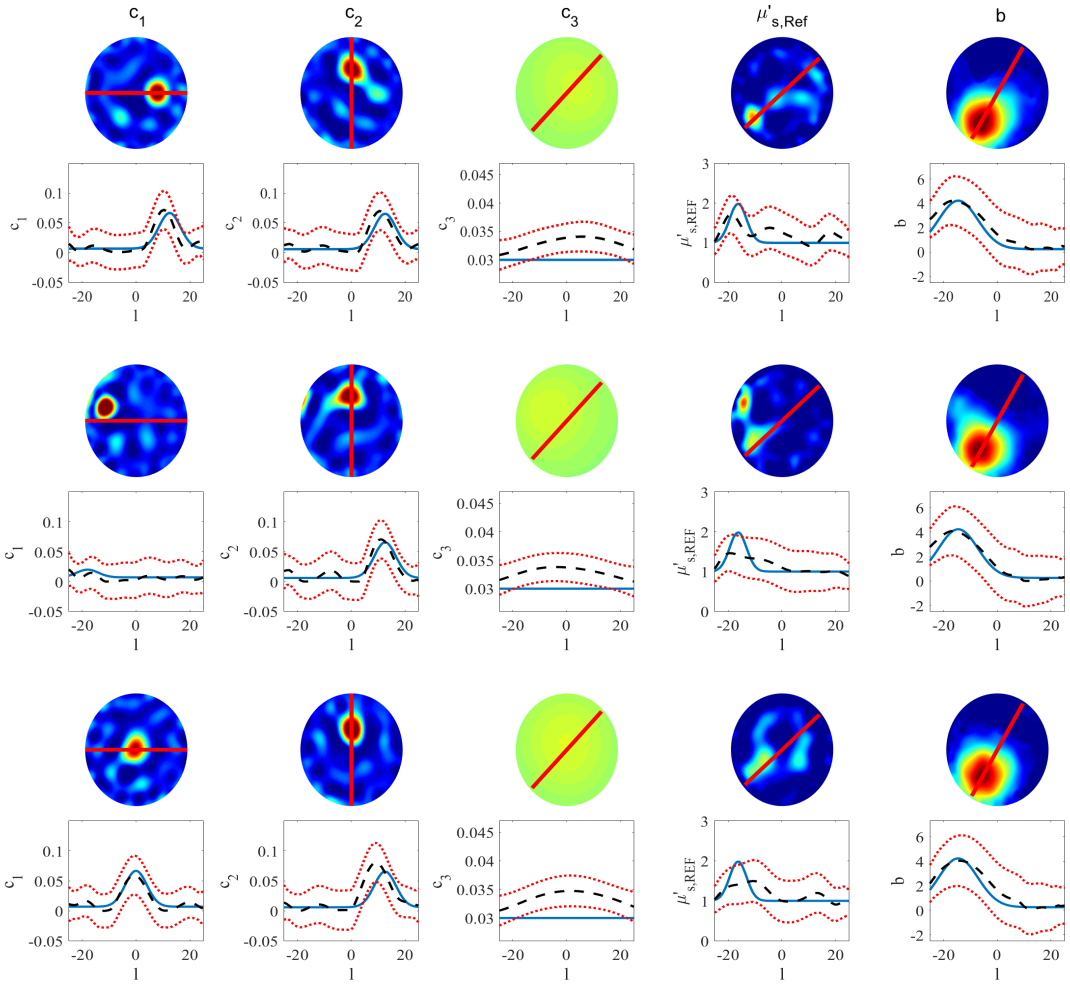

Figure 7: Varying inclusion position. Direct estimation reconstructions and cross-sectional graphs of oxygenated blood concentration c_1 (1st column), deoxygenated blood concentration c_2 (2nd column), fat concentration c_3 (3rd column), reference scattering coefficient $\mu'_{s,Ref}$ (4th column) and scattering power b (5th column) when background c_1 inclusion position is varied. The cross-sectional graphs display the true values as blue lines, estimated values as dashed lines and the credibility interval as red dotted lines.

Table 4: Relative errors RE (%) of estimated chromophore concentrations and scattering parameters in the approximation error modelling tests. The parameter c_1 is oxygenated blood concentration, c_2 is deoxygenated blood concentration, c_3 is fat concentration, $\mu'_{s,Ref}$ is reference scattering coefficient and b is scattering power. Reference denotes the reference case where the absorption coefficients were accurate. In cases $-$, ϵ_{λ_1}, and $\epsilon_{\lambda_{123}}$ the forward problem is solved using a 50% higher absorption coefficient for oxygenated blood (Inaccurate $\mu_{a,1}$) or for all chromophores (Inaccurate $\mu_{a,1}$, $\mu_{a,2}$ and $\mu_{a,3}$) at 800 nm compared to the inverse problem. The parameters are reconstructed using either no BAE correction ($-$) or using BAE correction (ϵ_{λ_1} and $\epsilon_{\lambda_{123}}$) where ϵ_{λ_1} and $\epsilon_{\lambda_{123}}$ represent two different sets of BAE statistics.

	RE_{c_1} (%)	RE_{c_2} (%)	RE_{c_3} (%)	$\mathrm{RE}_{\mu'_{s,\mathrm{Ref}}}$ (%)	RE_b (%)
Reference	51	51	9.4	14	39
Inaccurate $\mu_{a,1}$					
$-$	60	61	60	14	33
ϵ_{λ_1}	49	50	0.57	14	40
$\epsilon_{\lambda_{123}}$	52	59	0.23	7.9	19
Inaccurate $\mu_{a,1}$, $\mu_{a,2}$ and $\mu_{a,3}$					
$-$	67	72	110	15	35
ϵ_{λ_1}	49	50	0.62	14	40
$\epsilon_{\lambda_{123}}$	52	58	0.22	7.9	19

4.4.4 Varying the number of inclusions

Figure 8 shows the direct and two-step reconstructions when the number of inclusions was increased from 1 to 3. The relative errors of the estimates obtained using the single-stage approach are given in Table 3. Increasing the amount of c_1 inclusions exacerbated the cross-talk. Inclusions located close to each other had the tendency to appear as a single object. This is most likely due to the diffuse nature of the imaging modality, and could perhaps be slightly improved by utilising different prior information.

The Figure 9 shows the simulated parameters, directly estimated parameters and the credibility intervals of these estimates from Figure 8 respectively on a cross-sectional line across the target space. The cross-sectional graphs show that the direct estimates mostly fall within their credibility intervals.

4.4.5 Modelling of spectral uncertainties

Figure 10 shows direct reconstructions of parameters c_1, c_2, c_3, $\mu'_{s,\mathrm{Ref}}$ and b when the absorption coefficient of either only oxygenated blood at 800 nm or each chromophore at 800 nm was increased 50% and when the parameters were estimated with or without correcting them through BAE modelling. The corrected reconstructions were computed using either the ϵ_{λ_1} set or the $\epsilon_{\lambda_{123}}$ set as a basis for generating the approximation error statistics. Table 4 contains the relative errors for each estimated parameter.

As it can be seen, inaccurate approximation of absorption spectra causes approximation errors to occur in the reconstructions. Estimation errors were present whether the absorption spectrum inaccuracy occurred solely in the spectrum of oxygenated blood or consistently in the

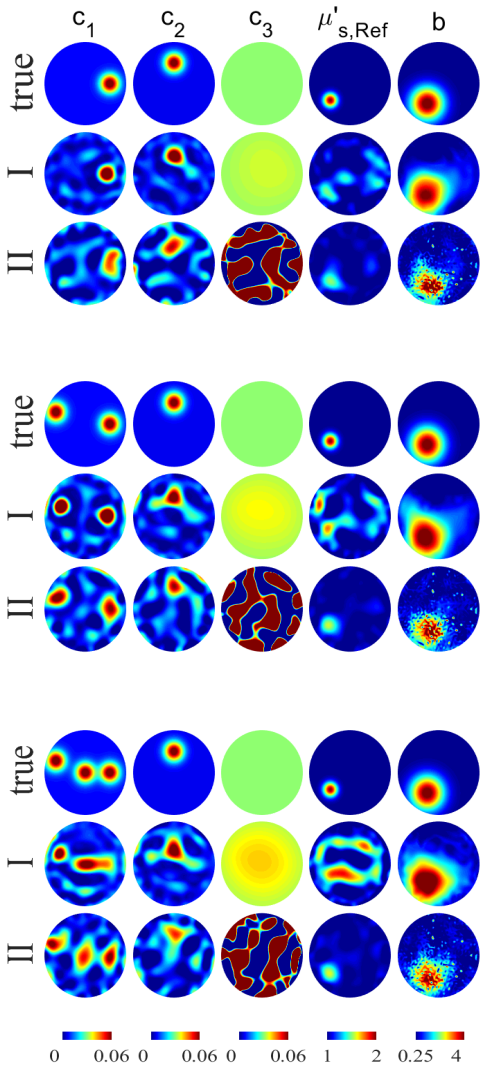

Figure 8: Varying number of inclusions. Simulated distributions (true) of oxygenated blood concentration c_1 (1st column), deoxygenated blood concentration c_2 (2nd column), fat concentration c_3 (3rd column), reference scattering coefficient $\mu'_{s,Ref}$ (4th column) and scattering power b (5th column) followed by direct estimation reconstructions (I) and two-step reconstructions (II) when the number of c_1 inclusions is varied.

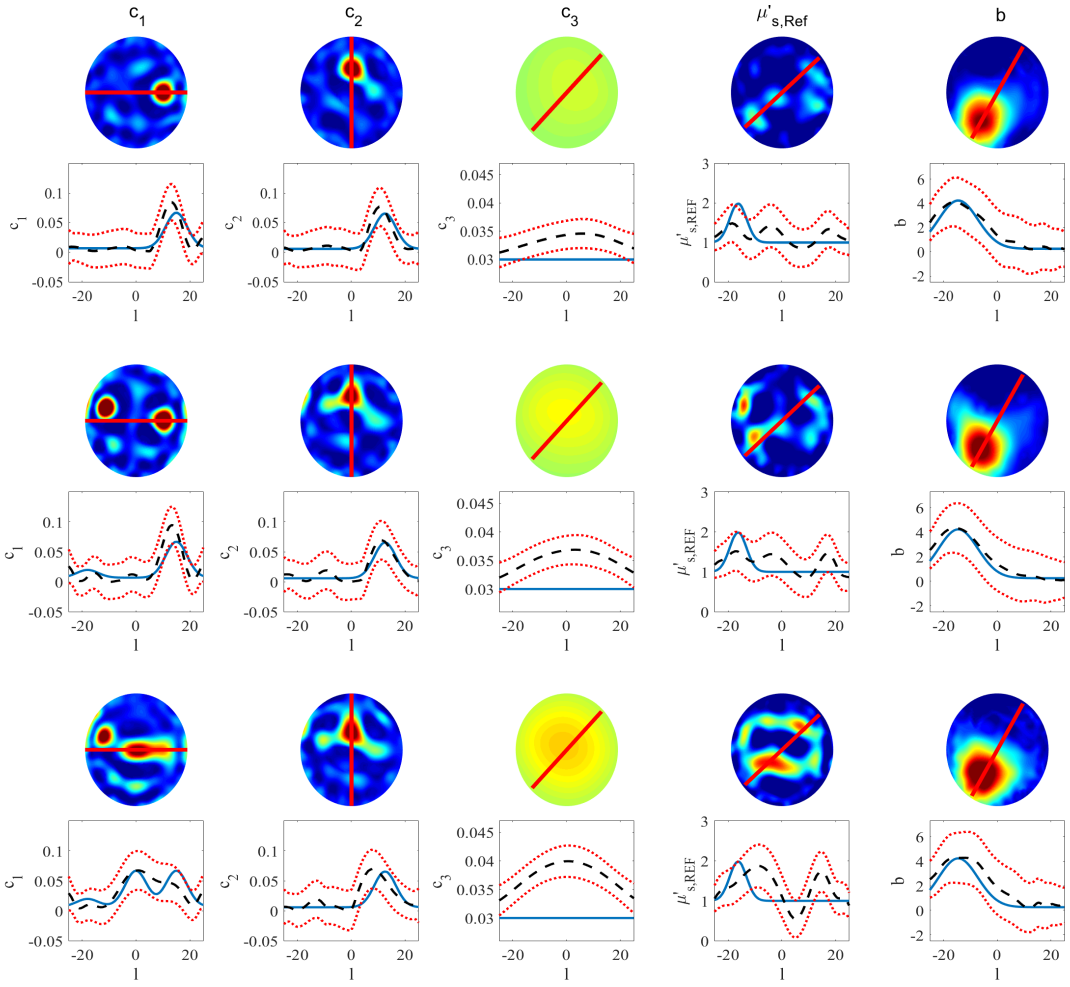

Figure 9: Varying number of inclusions. Direct estimation reconstructions and cross-sectional graphs of oxygenated blood concentration c_1 (1st column), deoxygenated blood concentration c_2 (2nd column), fat concentration c_3 (3rd column), reference scattering coefficient $\mu'_{s,Ref}$ (4th column) and scattering power b (5th column) when the number of c_1 inclusions is varied. The cross-sectional graphs display the true values as blue lines, estimated values as dashed lines and the credibility interval as red dotted lines.

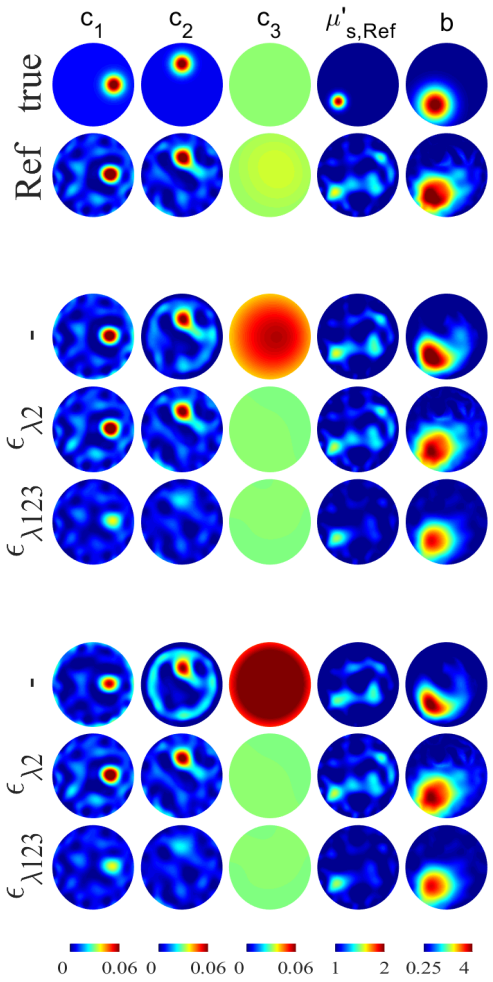

Figure 10: Simulated distributions of oxygenated blood concentration c_1, deoxygenated blood concentration c_2, fat concentration c_3, reference scattering coefficient $\mu'_{s,Ref}$ and scattering power b. The two top rows display the true values of the parameters and a reference case where the absorption coefficients were accurate. In cases $-$, ϵ_{λ_1}, and $\epsilon_{\lambda_{123}}$ the forward problem is solved using a 50% higher absorption coefficient for one chromophore that is oxygenated blood (3 middle rows) or for all chromophores (3 bottom rows) at 800 nm compared the inverse problem. The parameters are reconstructed using either no BAE correction ($-$) or using BAE correction (ϵ_{λ_1}, and $\epsilon_{\lambda_{123}}$) where ϵ_{λ_1} and $\epsilon_{\lambda_{123}}$ represent two different sets of BAE statistics.

spectra of all three chromophores. The estimation errors were reduced when BAE modelling was applied. The BAE corrected estimates were closer to the reference case and depicted the inclusions more accurately compared to cases where no BAE modelling was used or where ϵ_{λ_1} statistics were used instead of $\epsilon_{\lambda_{123}}$. The reconstructions generated using $\epsilon_{\lambda_{123}}$ statistics in Figure 10 showed lower contrast but less artefacts when compared to both the reconstruction without BAE modelling and the ϵ_{λ_1} reconstructions. The generation of the BAE statistics η_ϵ and Γ_ϵ involved simulating measurement data using uniformly sampled absorption coefficients. The results implied that the optimal BAE statistics are obtained when the sampling interval matches the true range of absorption spectrum deviations.

5 Discussion and conclusions

In this work the spectral DOT inverse problem was approached in a Bayesian framework. Concentrations of chromophores were directly estimated from simulated DOT data, and the reconstructions were compared to a two-stage approach where they were estimated from absorption reconstructions at multiple wavelengths. The reliability of the parameter estimates was evaluated by studying estimated credibility intervals. Furthermore, a Bayesian approximation error approach to model uncertainties in absorption spectra was proposed.

It was observed that the direct estimation approach was able to reconstruct simulated inclusions with higher accuracy than the two-step approach. This is consistent with prior spectral DOT studies and the projection that spectral implementation should decrease noise and reduce the ill-posedness of the problem [4]. The parameter estimates were found to settle within corresponding credibility intervals in most situations. This result is reasonable, because the estimates were expected to be within the credibility interval with a 99.7% likelihood.

When studying uncertainties in the absorption spectra, it was noticed that deviations in chromophore absorption spectra between data generation and image reconstruction caused a clear error in each of the reconstructions. It was further noticed that the Bayesian approximation error modelling successfully corrected these errors.

This work presents the first simulations utilising the Bayesian approach for spectral DOT. The results can be regarded to give a general idea of the performance of the approach. However, there are few other aspects that could be still studied and improved. For example in the simulations, modeling errors caused by discretisations could be potential source of errors in the reconstructions. In this work, the inverse crime was avoided by using different discretisations in the forward and inverse problems, and thus the results can be regarded reliable. However, finer discretisations could lead to improved image quality. Furthemore, in this work the forward model was the diffusion approximation. That is generally regarded as an accurate model in DOT. However, if the target domain would be smaller or in the presence of low-scattering inclusions, modelling light propagation using the radiative transfer equation would be required [10].

In order to study the proposed methodology more thoroughly, subsequent studies could investigate spectral DOT imaging with alternative source-detector configurations such as covering only a half of the boundary with sources and detectors, or decreasing or increasing the number of optical probes. In addition, different target sizes or ways to reduce cross-talk could be studied.

In conclusion, it was shown that a Bayesian approach to spectral DOT can be used to provide good quality reconstructions of chromophore concentrations and scattering parameters. Further, the methodology enables examining the reliability of these reconstructions and modelling uncertainties related to the absorption spectra.

Appendix

Appendix I

In order to derive the FE-approximation of the DA (6), we first derive the variational form of the DA and then formulate the FE-approximation. In order to derive the variational form, the diffusion approximation (6) is first multiplied by a test function $\psi(\vec{r})$ and integrated over the domain Ω.

$$\int_\Omega -\nabla\cdot\kappa(\vec{r})\nabla\phi(\vec{r},\omega)\psi(\vec{r})+\left[\mu_a(\vec{r})+\frac{\mathrm{i}\omega}{\mathrm{c}}\right]\phi(\vec{r},\omega)\psi(\vec{r})d\vec{r}=\int_\Omega q_0(\vec{r},\omega)\psi(\vec{r})d\vec{r} \tag{62}$$

The expression $\int_\Omega -\nabla\cdot\kappa(\vec{r})\nabla\phi(\vec{r},\omega)\psi(\vec{r})d\vec{r}$ is expanded using Green's second identity and substituted into equation (62), resulting in the equation

$$\begin{aligned}\int_\Omega \kappa(\vec{r})\nabla\phi(\vec{r},\omega)\cdot\nabla\psi(\vec{r})d\vec{r}-\int_{\partial\Omega}\kappa(\vec{r})\frac{\partial\phi(\vec{r},\omega)}{\partial\hat{n}}\psi(\vec{r})dS+\\ \int_\Omega\left[\mu_a(\vec{r})+\frac{\mathrm{i}\omega}{\mathrm{c}}\right]\phi(\vec{r},\omega)\psi(\vec{r})d\vec{r}=\int_\Omega q_0(\vec{r},\omega)\psi(\vec{r})d\vec{r}\end{aligned} \tag{63}$$

The term

$$\kappa(\vec{r})\frac{\partial\phi(\vec{r},\omega)}{\partial\hat{n}}=\frac{2\gamma}{\zeta}(q(\vec{r},\omega)-\phi(\vec{r},\omega)) \tag{64}$$

given by the boundary condition (7) is substituted into equation (63), resulting in

$$\begin{aligned}\int_\Omega \kappa(\vec{r})\nabla\phi(\vec{r},\omega)\cdot\nabla\psi(\vec{r})d\vec{r}-\int_{\partial\Omega}\frac{2\gamma}{\zeta}(q(\vec{r},\omega)-\phi(\vec{r},\omega))\psi(\vec{r})dS\\ +\int_\Omega\left[\mu_a(\vec{r})+\frac{\mathrm{i}\omega}{\mathrm{c}}\right]\phi(\vec{r},\omega)\psi(\vec{r})d\vec{r}=\int_\Omega q_0(\vec{r},\omega)\psi(\vec{r})d\vec{r}\end{aligned} \tag{65}$$

which can be rearranged, giving the variational form of the DA

$$\begin{aligned}\int_\Omega\kappa(\vec{r})\nabla\phi(\vec{r},\omega)\cdot\nabla\psi(\vec{r})+\left[\mu_a(\vec{r})+\frac{\mathrm{i}\omega}{\mathrm{c}}\right]\phi(\vec{r},\omega)\psi(\vec{r})d\vec{r}+\int_{\partial\Omega}\frac{2\gamma}{\zeta}\phi(\vec{r},\omega)\psi(\vec{r})dS\\ =\int_\Omega q_0(\vec{r},\omega)\psi(\vec{r})d\vec{r}+\int_{\partial\Omega}\frac{2\gamma}{\zeta}q(\vec{r},\omega)\psi(\vec{r})dS.\end{aligned} \tag{66}$$

To derive the FE-approximation, we approximate the photon density in a piecewise linear basis

$$\phi(\vec{r},\omega)=\sum_{j=1}^{N}\Phi_j(\omega)\varphi_j(\vec{r}), \tag{67}$$

where ϕ_j are finite element basis functions, and choose basis functions ϕ_i as test functions.

$$\psi(\vec{r})=\varphi_i(\vec{r}) \tag{68}$$

Furthermore, we approximate the absorption, scattering and diffusion in a piece-wise linear basis

$$\mu_a(\vec{r}) = \sum_{k=1}^{N} (\mu_a)_k \varphi_k(\vec{r}) \tag{69}$$

$$\mu_s'(\vec{r}) = \sum_{k=1}^{N} (\mu_s')_k \varphi_k(\vec{r}) \tag{70}$$

$$\kappa(\vec{r}) = \sum_{k=1}^{N} \kappa_k \varphi_k(\vec{r}). \tag{71}$$

If we use the collimated source model,

$$\int_{\partial\Omega} \frac{2\gamma}{\zeta} q(\vec{r},\omega)\varphi_k(\vec{r}) dS = 0, \tag{72}$$

equation (66) becomes

$$\begin{aligned} \sum_{j=1}^{N} \Bigg(\Bigg(\int_\Omega \sum_{k=1}^{N} \kappa_k \varphi_k(\vec{r}) \nabla\varphi_j(\vec{r}) \cdot \nabla\varphi_i(\vec{r}) + \Bigg[\sum_{k=1}^{N} (\mu_a)_k \varphi_k(\vec{r}) + \frac{\mathrm{i}\omega}{\mathrm{c}} \Bigg] \varphi_j(\vec{r})\varphi_i(\vec{r}) d\vec{r} \\ + \int_{\partial\Omega} \frac{2\gamma}{\zeta} \varphi_j(\vec{r})\varphi_i(\vec{r}) dS \Bigg) \Phi_j(\omega) \Bigg) = \int_\Omega q_0(\vec{r},\omega)\varphi_i(\vec{r}) d\vec{r} \end{aligned} \tag{73}$$

Further, the FE-approximation of the DA with a collimated source model can be written in the form

$$(K(\kappa(\vec{r})) + D(\mu_a(\vec{r})) + \frac{2\gamma}{\zeta} B + \mathrm{i}\omega C)\Phi(\omega) = Q(\omega) \tag{74}$$

where

$$K_{ij}(\kappa(\vec{r})) = \sum_{k=1}^{N} \kappa_k \int_\Omega \varphi_k(\vec{r}) \nabla\varphi_j(\vec{r}) \cdot \nabla\varphi_i(\vec{r}) d\vec{r} \tag{75}$$

$$D_{ij}(\mu_a(\vec{r})) = \sum_{k=1}^{N} (\mu_a)_k \int_\Omega \varphi_k(\vec{r})\varphi_j(\vec{r})\varphi_i(\vec{r}) d\vec{r} \tag{76}$$

$$C_{ij} = \frac{1}{\mathrm{c}} \int_\Omega \varphi_j(\vec{r})\varphi_i(\vec{r}) d\vec{r} \tag{77}$$

$$B_{ij} = \int_{\partial\Omega} \varphi_j(\vec{r})\varphi_i(\vec{r}) d\vec{r} \tag{78}$$

$$Q_{ij} = \int_\Omega q_0(\vec{r},\omega)\varphi_i(\vec{r}) d\vec{r} \tag{79}$$

Appendix II

The Jacobian matrix for the spectral DOT can be formulated as follows. The size of the Jacobian depends on the number of different wavelengths used in the measurements and the number of chromophores that are accounted for in modeling the absorption coefficient (33). For three wavelengths λ_1, λ_2 and λ_3 and three chromophores with concentrations c_1, c_2 and c_3, the Jacobian would consist of 15 blocks of Jacobian matrices corresponding to different chromophores and data at different wavelengths

$$\mathcal{J} = \begin{pmatrix} \frac{dF_{\lambda_1}}{dc_1} & \frac{dF_{\lambda_1}}{dc_2} & \frac{dF_{\lambda_1}}{dc_3} & \frac{dF_{\lambda_1}}{d\mu'_{s,\mathrm{Ref}}} & \frac{dF_{\lambda_1}}{db} \\ \frac{dF_{\lambda_2}}{dc_1} & \frac{dF_{\lambda_2}}{dc_2} & \frac{dF_{\lambda_2}}{dc_3} & \frac{dF_{\lambda_2}}{d\mu'_{s,\mathrm{Ref}}} & \frac{dF_{\lambda_2}}{db} \\ \frac{dF_{\lambda_3}}{dc_1} & \frac{dF_{\lambda_3}}{dc_2} & \frac{dF_{\lambda_3}}{dc_3} & \frac{dF_{\lambda_3}}{d\mu'_{s,\mathrm{Ref}}} & \frac{dF_{\lambda_3}}{db} \end{pmatrix}, \tag{80}$$

$\mathcal{J} \in \mathbb{R}^{3M\times 5N}$, where function F_{λ_k} is the forward operator of DOT as in equation (38) with wavelength set to $\lambda = \lambda_k$, $k \in \{1,\ 2,\ 3\}$. The chain rule expands the function $\frac{dF_{\lambda_k}}{dc_1}$ into a product

$$\frac{dF_{\lambda_k}}{dc_1} = \frac{dF_{\lambda_k}}{d\mu_a}\frac{d\mu_a}{dc_1}. \tag{81}$$

The differential function $\frac{dF_{\lambda_k}}{d\mu_a}$ is evaluated numerically and the function $\frac{d\mu_a}{dc_1}$ is

$$\begin{aligned} \frac{d\mu_a}{dc_1} &= \frac{d}{dc_1}(c_1\mu_{a,1} + c_2\mu_{a,2} + c_3\mu_{a,3}) && (82)\\ &= \frac{d}{dc_1}c_1\mu_{a,1} && (83)\\ &= \mu_{a,1}\frac{d}{dc_1}c_1 && (84)\\ &= \mu_{a,1}I_N && (85) \end{aligned}$$

Equation (81) becomes

$$\frac{dF_{\lambda_k}}{dc_1} = \frac{dF_{\lambda_k}}{d\mu_a}\mu_{a,1}I = \frac{dF_{\lambda_k}}{d\mu_a}\mu_{a,1} \tag{86}$$

Similarly, the functions $\frac{dF_{\lambda_k}}{dc_2}$ and $\frac{dF_{\lambda_k}}{dc_3}$ are

$$\begin{aligned} \frac{dF_{\lambda_k}}{dc_2} &= \frac{dF_{\lambda_k}}{d\mu_a}\mu_{a,2} && (87)\\ \frac{dF_{\lambda_k}}{dc_3} &= \frac{dF_{\lambda_k}}{d\mu_a}\mu_{a,3}. && (88) \end{aligned}$$

Chain rule for differential functions $\frac{dF_{\lambda_k}}{d\mu'_{s,\mathrm{Ref}}}$ and $\frac{dF_{\lambda_k}}{db}$ states that

$$\frac{dF_{\lambda_k}}{d\mu'_{s,Ref}} = \frac{dF_{\lambda_k}}{d\mu'_s}\frac{d\mu'_s}{d\mu'_{s,Ref}} \tag{89}$$

$$\frac{dF_{\lambda_k}}{db} = \frac{dF_{\lambda_k}}{d\mu'_s}\frac{d\mu'_s}{db}. \tag{90}$$

The differential function $\frac{dF_{\lambda_k}}{d\mu'_s}$ is evaluated numerically like the function $\frac{dF_{\lambda_k}}{d\mu_a}$. The j'th row and i'th column element of matrix $\frac{d\mu'_s}{d\mu'_{s,\mathrm{Ref}}}$ is

$$\frac{\partial \mu'_{s,i}}{\partial \mu'_{s,\mathrm{Ref},j}} = \frac{\partial}{\partial \mu'_{s,\mathrm{Ref},j}}\left(\mu'_{s,\mathrm{Ref},i}\left(\frac{\lambda_k}{\lambda_{\mathrm{Ref}}}\right)^{-b_i}\right) \tag{91}$$

$$= \begin{cases} 0, & j \neq i \\ \left(\frac{\lambda_k}{\lambda_{\mathrm{Ref}}}\right)^{-b_i}, & j = i \end{cases} \tag{92}$$

Matrix $\frac{d\mu'_s}{d\mu'_{s,\mathrm{Ref}}}$ is of the form

$$\frac{d\mu'_s}{d\mu'_{s,\mathrm{Ref}}} = \begin{pmatrix} \left(\frac{\lambda_k}{\lambda_{\mathrm{Ref}}}\right)^{-b_1} & 0 & \dots & 0 \\ 0 & \left(\frac{\lambda_k}{\lambda_{\mathrm{Ref}}}\right)^{-b_2} & \dots & 0 \\ \vdots & \vdots & \ddots & \vdots \\ 0 & 0 & \dots & \left(\frac{\lambda_k}{\lambda_{\mathrm{Ref}}}\right)^{-b_N} \end{pmatrix} \tag{93}$$

and function $\frac{dF_{\lambda_k}}{d\mu'_{s,\mathrm{Ref}}}$ in equation (89) is consequently

$$\frac{dF_{\lambda_k}}{d\mu'_{s,\mathrm{Ref}}} = \frac{dF_{\lambda_k}}{d\mu'_s}\begin{pmatrix} \left(\frac{\lambda_k}{\lambda_{\mathrm{Ref}}}\right)^{-b_1} & 0 & \dots & 0 \\ 0 & \left(\frac{\lambda_k}{\lambda_{\mathrm{Ref}}}\right)^{-b_2} & \dots & 0 \\ \vdots & \vdots & \ddots & \vdots \\ 0 & 0 & \dots & \left(\frac{\lambda_k}{\lambda_{\mathrm{Ref}}}\right)^{-b_N} \end{pmatrix}. \tag{94}$$

The j'th row and i'th column element of matrix $\frac{d\mu'_s}{db}$ is

$$\frac{\partial \mu'_{s,i}}{\partial b_j} = \frac{\partial}{\partial b_j}\left(\mu'_{s,\mathrm{Ref},i}\left(\frac{\lambda_k}{\lambda_{\mathrm{Ref}}}\right)^{-b_i}\right) \tag{95}$$

$$= \begin{cases} 0, & j \neq i \\ -\mu'_{s,\mathrm{Ref},i}\ln\left(\frac{\lambda_k}{\lambda_{\mathrm{Ref}}}\right)\left(\frac{\lambda_k}{\lambda_{\mathrm{Ref}}}\right)^{-b_i}, & j = i \end{cases} \tag{96}$$

and the complete matrix is

$$\frac{d\mu'_s}{db} = \begin{pmatrix} -\mu'_{s,\mathrm{Ref},1} \ln\left(\frac{\lambda_k}{\lambda_{\mathrm{Ref}}}\right)\left(\frac{\lambda_k}{\lambda_{\mathrm{Ref}}}\right)^{-b_1} & \cdots & 0 \\ \vdots & \ddots & \vdots \\ 0 & \cdots & -\mu'_{s,\mathrm{Ref},N} \ln\left(\frac{\lambda_k}{\lambda_{\mathrm{Ref}}}\right)\left(\frac{\lambda_k}{\lambda_{\mathrm{Ref}}}\right)^{-b_N} \end{pmatrix} \tag{97}$$

Equation (90) takes the form

$$\frac{dF_{\lambda_k}}{db} = \frac{dF_{\lambda_k}}{d\mu'_s} \ln\left(\frac{\lambda_k}{\lambda_{\mathrm{Ref}}}\right) \begin{pmatrix} -\mu'_{s,\mathrm{Ref},1}\left(\frac{\lambda_k}{\lambda_{\mathrm{Ref}}}\right)^{-b_1} & \cdots & 0 \\ \vdots & \ddots & \vdots \\ 0 & \cdots & -\mu'_{s,\mathrm{Ref},N}\left(\frac{\lambda_k}{\lambda_{\mathrm{Ref}}}\right)^{-b_N} \end{pmatrix}. \tag{98}$$

Appendix III

Figure 11 shows both the direct and the two-step reconstructions of c_1, c_2, c_3, $\mu'_{s,\mathrm{Ref}}$ and b with different simulated deoxygenated blood background values $c_{2,b}$. Figures 12 and 13 display the direct and two-step reconstructions of the parameter distributions when inclusion magnitudes of oxygenated blood and deoxygenated blood, respectively, are varied. These additional simulations support the finding that $\mu'_{s,\mathrm{Ref}}$ cross-talk is reduced when the true inclusion-to-background contrast of a chromophore concentration is lower.

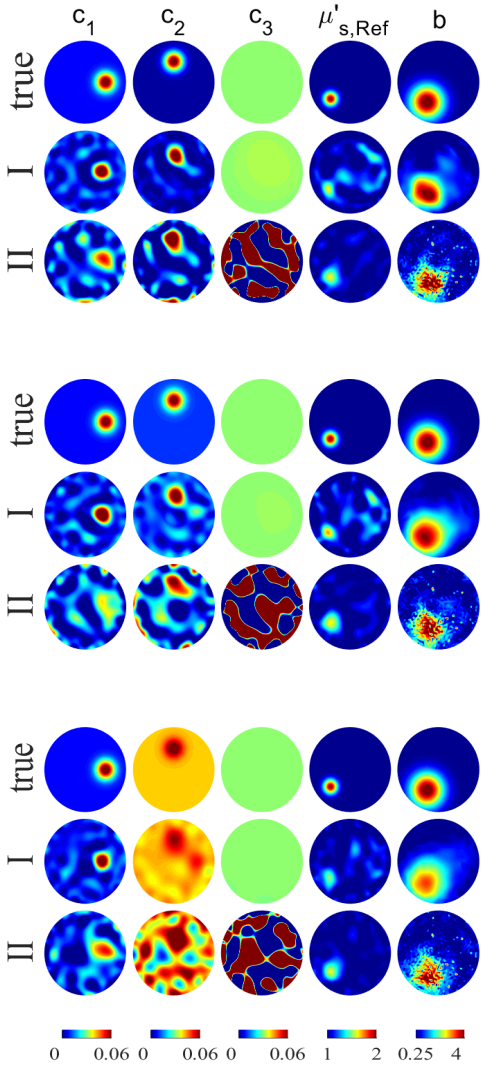

Figure 11: Varying background values of distribution c_2. Simulated distributions (true) of oxygenated blood concentration c_1 (1st column), deoxygenated blood concentration c_2 (2nd column), fat concentration c_3 (3rd column), reference scattering coefficient $\mu'_{s,Ref}$ (4th column) and scattering power b (5th column) followed by direct estimation reconstructions (I) and two-step reconstructions (II) when background deoxygenated blood concentration $c_{2,b}$ is varied. In the top three rows, background value of deoxygenated blood concentration was 0.001, in the next three rows 0.01 and in the last three rows 0.04.

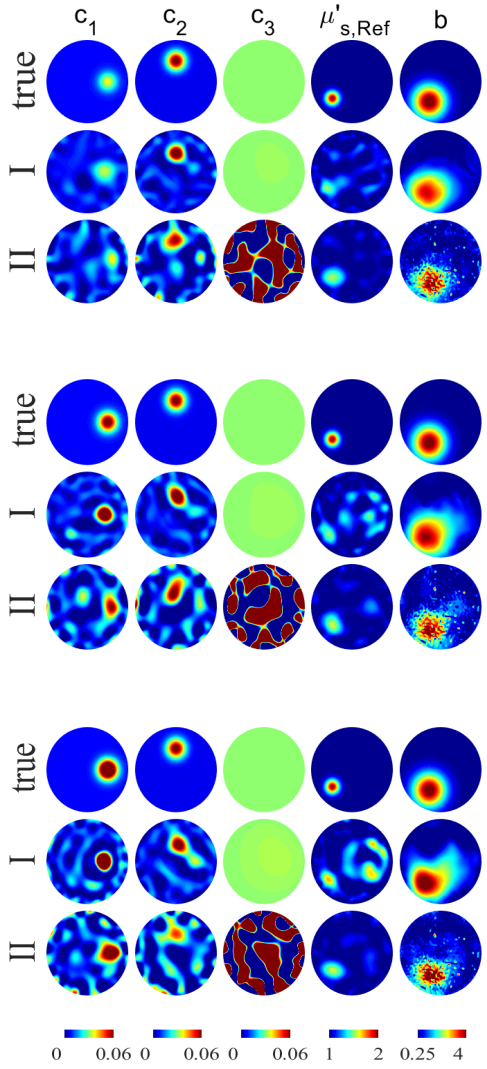

Figure 12: Varying c_1 inclusion magnitude. Simulated distributions (true) of oxygenated blood concentration c_1 (1st column), deoxygenated blood concentration c_2 (2nd column), fat concentration c_3 (3rd column), reference scattering coefficient $\mu'_{s,Ref}$ (4th column) and scattering power b (5th column) followed by direct estimation reconstructions (I) and two-step reconstructions (II) when oxygenated blood concentration at the inclusion is varied. In the top three rows, the inclusion magnitude of oxygenated blood is 0.3, in the next three rows 0.6 and in the last three rows 0.9.

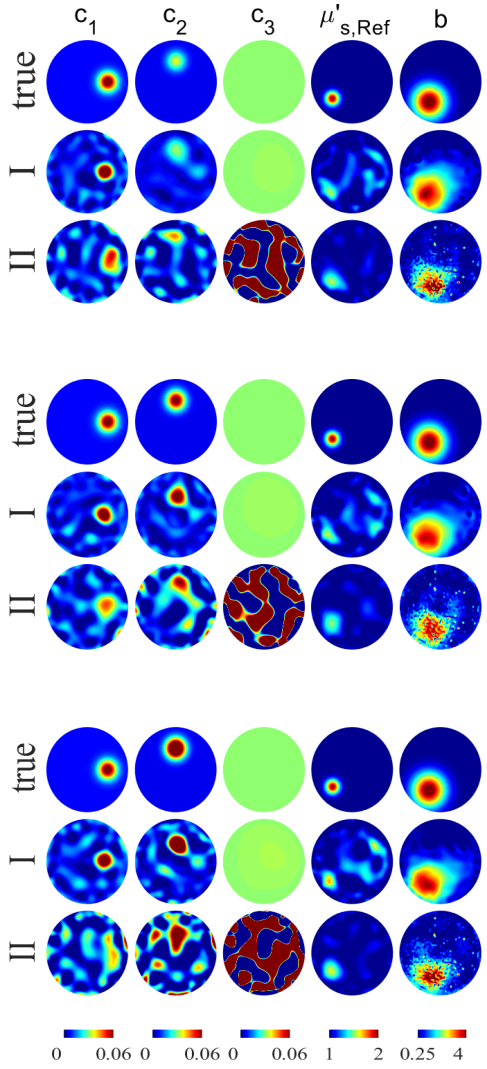

Figure 13: Varying c_2 inclusion magnitude. Simulated distributions (true) of oxygenated blood concentration c_1 (1st column), deoxygenated blood concentration c_2 (2nd column), fat concentration c_3 (3rd column), reference scattering coefficient $\mu'_{s,Ref}$ (4th column) and scattering power b (5th column) followed by direct estimation reconstructions (I) and two-step reconstructions (II) when deoxygenated blood concentration at the inclusion is varied. In the top three rows, the inclusion magnitude of deoxygenated blood is 0.3, in the next three rows 0.6 and in the last three rows 0.9.

References

[1] A. P. Gibson, J. C. Hebden, and S. R. Arridge, "Recent advances in diffuse optical imaging," *Physics in Medicine & Biology*, vol. 50, no. 4, R1, 2005.

[2] C. Li, H. Zhao, B. Anderson, and H. Jiang, "Multispectral breast imaging using a ten-wavelength, source/detector channels silicon photodiode-based diffuse optical tomography system," *Medical Physics*, vol. 33, no. 3, pp. 627–636, 2006.

[3] A. Corlu, T. Durduran, R. Choe, M. Schweiger, E. M. Hillman, S. R. Arridge, and A. G. Yodh, "Uniqueness and wavelength optimization in continuous-wave multispectral diffuse optical tomography," *Optics Letters*, vol. 28, no. 23, pp. 2339–2341, 2003.

[4] S. Srinivasan, B. W. Pogue, S. Jiang, H. Dehghani, and K. D. Paulsen, "Spectrally constrained chromophore and scattering near-infrared tomography provides quantitative and robust reconstruction," *Applied Optics*, vol. 44, no. 10, pp. 1858–1869, 2005.

[5] B. Brendel and T. Nielsen, "Wavelengths optimization in multi spectral diffuse optical tomography considering uncertainties in absorption spectra," in *European Conferences on Biomedical Optics*, Optical Society of America, 2007.

[6] S. R. Arridge, "Optical tomography in medical imaging," *Inverse Problems*, vol. 15, no. 2, R41, 1999.

[7] J. C. Hebden and T. Austin, "Optical tomography of the neonatal brain," *European Radiology*, vol. 17, no. 11, pp. 2926–2933, 2007.

[8] J. C. Hebden and D. T. Delpy, "Enhanced time-resolved imaging with a diffusion model of photon transport," *Optics Letters*, vol. 19, no. 5, pp. 311–313, 1994.

[9] M. Mozumder, T. Tarvainen, A. Seppänen, I. Nissilä, S. R. Arridge, and V. Kolehmainen, "Nonlinear approach to difference imaging in diffuse optical tomography," *Journal of Biomedical Optics*, vol. 20, no. 10, p. 105 001, 2015.

[10] T. Tarvainen, "Computational methods for light transport in optical tomography," Ph.D. dissertation, Kuopio University, 2006.

[11] W. West, "Absorption of electromagnetic radiation," *AccessScience,© McGraw-Hill Companies*, 2008.

[12] J. Tervo, P. Kolmonen, M. Vauhkonen, L. Heikkinen, and J. Kaipio, "A finite-element model of electron transport in radiation therapy and a related inverse problem," *Inverse Problems*, vol. 15, no. 5, p. 1345, 1999.

[13] L. G. Henyey and J. L. Greenstein, "Diffuse radiation in the galaxy," *The Astrophysical Journal*, vol. 93, pp. 70–83, 1941.

[14] L. V. Wang and H. Wu, *Biomedical Optics: Principles and Imaging*. John Wiley & Sons, 2007.

[15] M. Mozumder, "Image reconstruction with error modelling in diffuse optical tomography," Ph.D. dissertation, University of Eastern Finland, 2015.

[16] M. Schweiger and S. R. Arridge, "The Toast++ software suite for forward and inverse modeling in optical tomography," *Journal of Biomedical Optics*, vol. 19, no. 4, p. 040 801, 2014.

[17] S. Arridge, M. Schweiger, M. Hiraoka, and D. Delpy, "A finite element approach for modeling photon transport in tissue," *Medical Physics*, vol. 20, no. 2, pp. 299–309, 1993.

[18] J. C. Hebden, "Advances in optical imaging of the newborn infant brain," *Psychophysiology*, vol. 40, no. 4, pp. 501–510, 2003.

[19] D. A. Benaron, S. R. Hintz, A. Villringer, D. Boas, A. Kleinschmidt, J. Frahm, C. Hirth, H. Obrig, J. C. van Houten, E. L. Kermit, *et al.*, "Noninvasive functional imaging of human brain using light," *Journal of Cerebral Blood Flow & Metabolism*, vol. 20, no. 3, pp. 469–477, 2000.

[20] T. Zhang, J. Yang, J. Zhou, H. Yang, P. R. Carney, and H. Jiang, "Real-time multispectral diffuse optical tomography system for imaging epileptic activity and connectivity," in *Design and Quality for Biomedical Technologies VI*, International Society for Optics and Photonics, vol. 8573, 2013, p. 857 305.

[21] A. T. Eggebrecht, S. L. Ferradal, A. Robichaux-Viehoever, M. S. Hassanpour, H. Dehghani, A. Z. Snyder, T. Hershey, and J. P. Culver, "Mapping distributed brain function and networks with diffuse optical tomography," *Nature Photonics*, vol. 8, no. 6, pp. 448–454, 2014.

[22] J. C. Hebden, A. Gibson, R. M. Yusof, N. Everdell, E. M. Hillman, D. T. Delpy, S. R. Arridge, T. Austin, J. H. Meek, and J. S. Wyatt, "Three-dimensional optical tomography of the premature infant brain," *Physics in Medicine & Biology*, vol. 47, no. 23, p. 4155, 2002.

[23] M. Chalia, L. A. Dempsey, R. J. Cooper, C.-W. Lee, A. P. Gibson, J. C. Hebden, and T. Austin, "Diffuse optical tomography for the detection of perinatal stroke at the cot side: A," *Stroke*, vol. 14, no. 5, pp. 299–310, 2009.

[24] H. Dehghani, B. W. Pogue, S. P. Poplack, and K. D. Paulsen, "Multiwavelength three-dimensional near-infrared tomography of the breast: Initial simulation, phantom, and clinical results," *Applied Optics*, vol. 42, no. 1, pp. 135–145, 2003.

[25] R. Choe, S. D. Konecky, A. Corlu, K. Lee, T. Durduran, D. R. Busch Jr, S. Pathak, B. J. Czerniecki, J. C. Tchou, D. L. Fraker, *et al.*, "Differentiation of benign and malignant breast tumors by in-vivo three-dimensional parallel-plate diffuse optical tomography," *Journal of Biomedical Optics*, vol. 14, no. 2, p. 024 020, 2009.

[26] M. Patachia, D. Dutu, and D. Dumitras, "Blood oxygenation monitoring by diffuse optical tomography," *IOP Publishing*, vol. 40, no. 12, pp. 1062–1066, Jan. 2011.

[27] L. Enfield, G. Cantanhede, M. Douek, V. Ramalingam, A. Purushotham, J. C. Hebden, and A. P. Gibson, "Monitoring the response to neoadjuvant hormone therapy for locally advanced breast cancer using three-dimensional time-resolved optical mammography," *Journal of Biomedical Optics*, vol. 18, no. 5, p. 056 012, 2013.

[28] D. Lighter, J. Hughes, I. Styles, A. Filer, and H. Dehghani, "Multispectral, non-contact diffuse optical tomography of healthy human finger joints," *Biomedical Optics Express*, vol. 9, no. 4, pp. 1445–1460, 2018.

[29] Y. Xu, N. Iftimia, H. Jiang, L. L. Key, and M. B. Bolster, "Imaging of in vitro and in vivo bones and joints with continuous-wave diffuse optical tomography," *Optics Express*, vol. 8, no. 7, pp. 447–451, 2001.

[30] H. Y. Wu, A. Filer, I. Styles, and H. Dehghani, "Development of a multi-wavelength diffuse optical tomography system for early diagnosis of rheumatoid arthritis: Simulation, phantoms and healthy human studies," *Biomedical Optics Express*, vol. 7, no. 11, pp. 4769–4786, 2016.

[31] H. Zhao, F. Gao, Y. Tanikawa, K. Homma, and Y. Yamada, "Time-resolved diffuse optical tomographic imaging for the provision of both anatomical and functional information about biological tissue," *Applied Optics*, vol. 44, no. 10, pp. 1905–1916, 2005.

[32] A. Pulkkinen, B. T. Cox, S. R. Arridge, J. P. Kaipio, and T. Tarvainen, "A Bayesian approach to spectral quantitative photoacoustic tomography," *Inverse Problems*, vol. 30, no. 6, p. 065 012, 2014.

[33] N. Hänninen, A. Pulkkinen, and T. Tarvainen, "Image reconstruction with reliability assessment in quantitative photoacoustic tomography," *Journal of Imaging*, vol. 4, no. 12, p. 148, 2018.

[34] C. K. Williams and C. E. Rasmussen, *Gaussian Processes for Machine Learning*. MIT Press Cambridge, MA, 2006, vol. 2.

[35] M. Schweiger, S. R. Arridge, and I. Nissilä, "Gauss–Newton method for image reconstruction in diffuse optical tomography," *Physics in Medicine & Biology*, vol. 50, no. 10, p. 2365, 2005.

[36] S. R. Arridge, "Methods in diffuse optical imaging," *Philosophical Transactions of the Royal Society A: Mathematical, Physical and Engineering Sciences*, vol. 369, no. 1955, pp. 4558–4576, 2011.

[37] W. Lu, D. Lighter, and I. B. Styles, "L_1-norm based nonlinear reconstruction improves quantitative accuracy of spectral diffuse optical tomography," *Biomedical Optics Express*, vol. 9, no. 4, pp. 1423–1444, 2018.

[38] Y. Zhan, A. T. Eggebrecht, J. P. Culver, and H. Dehghani, "Singular value decomposition based regularization prior to spectral mixing improves crosstalk in dynamic imaging using spectral diffuse optical tomography," *Biomedical Optics Express*, vol. 3, no. 9, pp. 2036–2049, 2012.

[39] J. Feng, S. Jiang, J. Xu, Y. Zhao, B. W. Pogue, and K. D. Paulsen, "Multiobjective guided priors improve the accuracy of near-infrared spectral tomography for breast imaging," *Journal of Biomedical Optics*, vol. 21, no. 9, p. 090 506, 2016.

[40] A. Li, E. L. Miller, M. E. Kilmer, T. J. Brukilacchio, T. Chaves, J. Stott, Q. Zhang, T. Wu, M. Chorlton, R. H. Moore, *et al.*, "Tomographic optical breast imaging guided by three-dimensional mammography," *Applied Optics*, vol. 42, no. 25, pp. 5181–5190, 2003.

[41] A. Li, G. Boverman, Y. Zhang, D. Brooks, E. L. Miller, M. E. Kilmer, Q. Zhang, E. M. Hillman, and D. A. Boas, "Optimal linear inverse solution with multiple priors in diffuse optical tomography," *Applied Optics*, vol. 44, no. 10, pp. 1948–1956, 2005.

[42] J. Zouaoui, L. Di Sieno, L. Hervé, A. Pifferi, A. Farina, A. Dalla Mora, J. Derouard, and J.-M. Dinten, "Chromophore decomposition in multispectral time-resolved diffuse optical tomography," *Biomedical Optics Express*, vol. 8, no. 10, pp. 4772–4787, 2017.

[43] E. Ferocino, G. Di Sciacca, L. Di Sieno, A. Dalla Mora, A. Pifferi, S. Arridge, F. Martelli, P. Taroni, and A. Farina, "Spectral approach to time domain diffuse optical tomography for breast cancer: Validation on meat phantoms," in *European Conferences on Biomedical Optics*, Optical Society of America, 2019.

[44] C. Li, S. R. Grobmyer, L. Chen, Q. Zhang, L. L. Fajardo, and H. Jiang, "Multispectral diffuse optical tomography with absorption and scattering spectral constraints," *Applied Optics*, vol. 46, no. 34, pp. 8229–8236, 2007.

[45] H. Dehghani, F. Leblond, B. W. Pogue, and F. Chauchard, "Application of spectral derivative data in spectral near infrared tomography," in *Optical Tomography and Spectroscopy of Tissue IX*, International Society for Optics and Photonics, vol. 7896, 2011, p. 78960I.

[46] H. Xu, B. W. Pogue, R. Springett, and H. Dehghani, "Spectral derivative based image reconstruction provides inherent insensitivity to coupling and geometric errors," *Optics Letters*, vol. 30, no. 21, pp. 2912–2914, 2005.

[47] S. Srinivasan, B. W. Pogue, H. Dehghani, F. Leblond, and X. Intes, "Data subset algorithm for computationally efficient reconstruction of 3-d spectral imaging in diffuse optical tomography," *Optics Express*, vol. 14, no. 12, pp. 5394–5410, 2006.

[48] A. Corlu, R. Choe, T. Durduran, K. Lee, M. Schweiger, S. R. Arridge, E. M. Hillman, and A. G. Yodh, "Diffuse optical tomography with spectral constraints and wavelength optimization," *Applied Optics*, vol. 44, no. 11, pp. 2082–2093, 2005.

[49] M. E. Eames, J. Wang, B. W. Pogue, and H. Dehghani, "Wavelength band optimization in spectral near-infrared optical tomography improves accuracy while reducing data acquisition and computational burden," *Journal of Biomedical Optics*, vol. 13, no. 5, p. 054 037, 2008.

[50] M. Mozumder, T. Tarvainen, S. R. Arridge, J. Kaipio, and V. Kolehmainen, "Compensation of optode sensitivity and position errors in diffuse optical tomography using the approximation error approach," *Biomedical Optics Express*, vol. 4, no. 10, pp. 2015–2031, 2013.

[51] J. Tick, A. Pulkkinen, and T. Tarvainen, "Modelling of errors due to speed of sound variations in photoacoustic tomography using a Bayesian framework," *Biomedical Physics & Engineering Express*, vol. 6, no. 1, p. 015 003, 2019.